APPLICATION OF POLARIZED EXAFS TO FINE-GRAINED LAYERED MINERALS

A. MANCEAU, M. SCHLEGEL, D. CHATEIGNER,
B. LANSON, C. BARTOLI, W. GATES

CONTENTS

in CMS Workshop Lectures, Vol.9, Synchrotron Methods in Clay Science, Schulze, D.G., Stucki, J.W., and Bertsch, P.M. eds. (1999), The Clay Minerals Society, Boulder, CO, p. 68-114.

APPLICATION OF POLARIZED EXAFS TO FINE-GRAINED LAYERED MINERALS

A. Manceau[1], M. Schlegel[1], D. Chateigner[2],

B. Lanson[1], C. Bartoli[1], W. Gates[1,*]

[1] Environmental Geochemistry Group, LGIT-IRIGM, University Joseph Fourier and CNRS, 38041 Grenoble Cedex 9, France

[2] Laboratoire de Physique de l'Etat Condensé, Université du Maine-Le Mans, avenue O. Messiaen, BP535 72085 Le Mans cedex, France

* Present address: CSIRO Land and Water, Glen Osmond, SA 5064, Australia

INTRODUCTION

This chapter describes the new possibilities offered by application of polarized EXAFS (P-EXAFS) spectroscopy to structural studies of fine-grained layered minerals. X-rays delivered by synchrotron sources are more than 95% polarized in the central part of the plane of rotation of the synchrotron electrons, and the polarization rate is further increased because of the polarization that occurs during monochromation of the incident beam. Because of the highly polarized nature of synchrotron radiation, one can obtain angularly resolved structural information through analysis of the angular dependence of X-ray absorption spectra for anisotropic samples. Originally, this technique was applied to single phyllosilicate crystals (Manceau et al. 1988; Manceau et al. 1990), and we show here that it can be extended to self-supporting films of fine-grained layered minerals. The angular variation of P-EXAFS spectra sensitively depends on the orientation distribution of individual mineral platelets in the prepared film. In the case of smectites, highly oriented films can be prepared, which allows us to precisely probe their 3-dimensional local structure without loss of spatial resolution as compared to single crystals.

LIMITATION OF POWDER EXAFS SPECTROSCOPY

Overlap of Atomic Shell Contributions

Application of EXAFS to mineralogy is often limited by the strong overlap of scattering contributions from neighboring atomic shells surrounding the X-ray absorber. This problem is illustrated in Figure 1a which compares the radial structure functions (RSFs) for nickeliferous talc [Si_4 $Ni_3O_{10}(OH)_2$], nickeliferous serpentine [$Si_2Ni_3O_5(OH)_4$], and $Ni(OH)_2$. These RSFs have a contrasted second peak amplitude even though in these three structures Ni atoms are surrounded by 6 Ni at about the same distance of $b/3 \sim 3.05$ Å (Figure 1b). Manceau (1990) showed that the difference in peak intensities resulted from an in-phase contribution of the nearest Si shell (Si_1) located just beyond the Ni shell at ~3.25Å. The difference in peak magnitude between talc and serpentine arises from the fact that in a TOT framework each octahedral cation (Oct) is bridged to four nearest tetrahedral cations (Tet), whereas it is bridged to two in a TO framework (Figure 1b). It turns out that in phyllosilicates the nearest EXAFS contribution from the tetrahedral sheet(s) is dominated by an overlapping contribution from the octahedral sheet, and the resulting omission of the tetrahedral contribution during spectral analysis (Fukushima and Okamoto 1987; Guttler et al. 1989) leads to an overestimation of the number of octahedral pairs (N_{Oct}). Table 1 shows that in clay structures the overlap between sucessive atomic shells increases with distance from the central atom, and this is one reason why, with few exceptions (Manceau et al. 1998; O'Day et al. 1994), the quantitative spectral analysis of layered clay minerals has been previously limited to the three nearest shells (Oct-O, Oct-Oct_1, Oct-Tet_1) located below ~ 3.3 Å. We will show below that this limit can be extended in P-EXAFS experiments because the contributions from the out-of plane tetrahedral cations are minimized when the X-ray polarization vector is in the ab plane of the layer (parallel orientation) and, conversely, the contributions from octahedral layer cations vanish when the polarization vector is aligned along the [001]* direction (normal oreintation).

Table 1. Successive atomic shells and interatomic distances from Fe in Garfield nontronite. After Manceau et al. (1998).

Shell	Distance (Å)	Shell	Distance (Å)	Shell	Distance (Å)
O_1 (x6)	1.97-2.04	O_5 (x2)	4.44	Fe_2 (x6)	5.28
Fe_1 (x3)	3.05	$(Si,Al)_2$ (x4)	4.49	$(Si,Al)_3$ (x8)	5.38-5.45
$(Si,Al)_1$ (x4)	3.26	O_6 (x8)	4.60-4.70	O_9 (x6)	5.72-6.02
O_2 (x2)	3.45	O_7 (x4)	4.83-4.89	Na_2 (x2)	5.93
O_3 (x6)	3.74-3.82	O_8 (x6)	4.94-4.98	Fe_3 (x3)	6.10
O_4 (x4)	4.03-4.21	Na_1 (x2)	5.12		

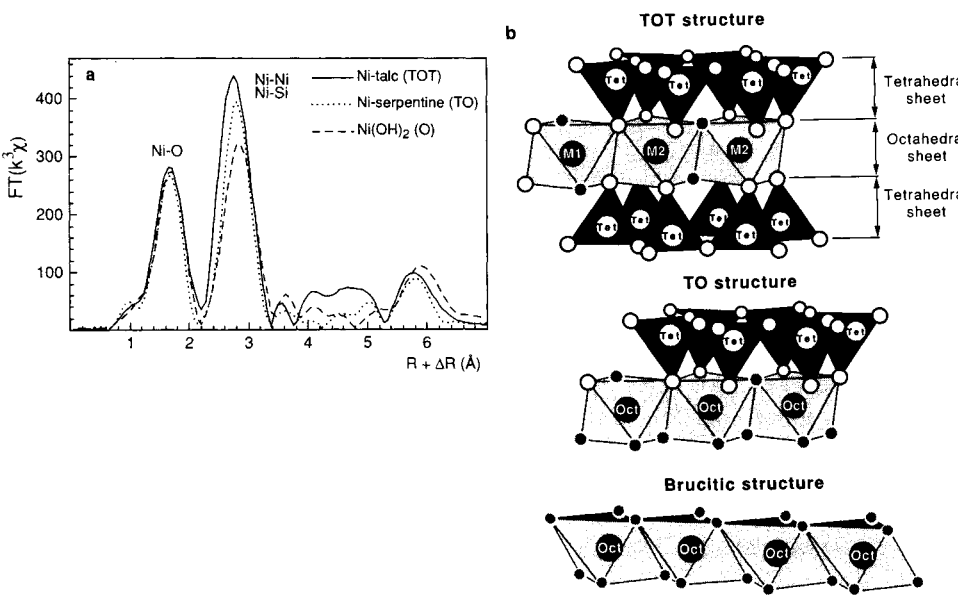

Figure 1. a) Radial structure functions of Ni-talc, Ni-serpentine, and $Ni(OH)_2$. b) Idealized structures of 2:1 and 1:1 phyllosilicate and brucitic layers. M1 denotes *trans*-sites and M2 *cis* -sites. Oct and Tet denote, respectively, octahedral and tetrahedral cations.

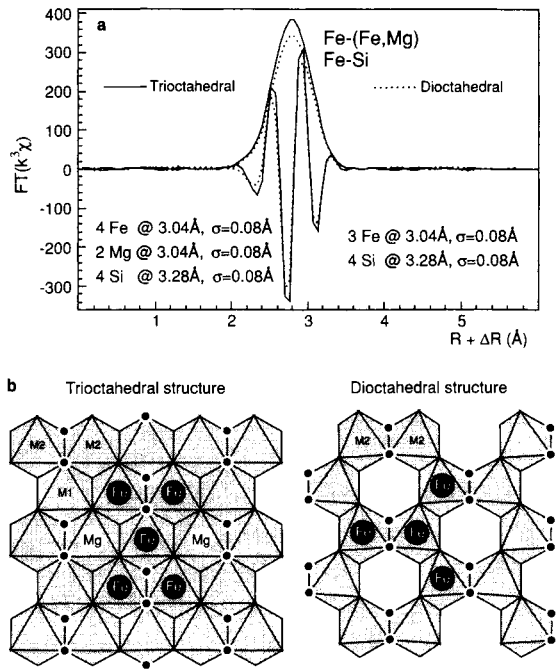

Figure 2. a) Fourier transforms of the EXAFS contributions calculated for 3 Fe at 3.04 Å and 4 Fe + 2 Mg at R = 3.04 Å. The envelope curves represent the magnitude of the transforms (RSF=$[Im(FT)^2+Re(FT)^2]^{1/2}$) and the fast oscillatory curves represent the imaginary parts of the transforms. b) Projection down c* of the octahedral sheet where a central Fe atom is surrounded by 4Fe + 2Mg atoms (trioctahedral structure, e.g., biotite) or 3Fe atoms (dioctahedral structure, e.g., nontronite).

Differentiation Between Dioctahedral and Trioctahedral Frameworks

In trioctahedral structures, all octahedral positions are occupied, whereas only 2/3 of all available sites are occupied in dioctahedral structures (Figure 2b). Octahedral cations are surrounded by 6 Oct in trioctahedral structures, and 3 Oct in dioctahedral structures and, consequently, these two groups of minerals should have distinctly different second RSF peak magnitude, allowing their differentiation. For certain chemical compositions this is not true as illustrated in Figure 2a. Figure 2 compares the Fourier transforms (modulus and imaginary part) calculated for a dioctahedral local environment consisting of 3 Fe^{3+} with a trioctahedral environment consisting of 4 Fe^{2+} +

2 Mg/Al. It is striking to observe that these two contrasting chemical compositions (and layer structure types) lead to practically the same result. A combination of two factors are responsible for this result. First, Mg and Al atoms both have approximately half the electrons as Fe, thus their scattering amplitude is halved, so 2 Mg give the same amplitude as 1 Fe. Second, the electronic waves backscattered by Mg and Al are shifted out of phase by π relative to that of Fe (McKale et al. 1988). Consequently, in trioctahedral structures, each contribution of two Mg atoms subtracts from the contribution of one Fe, and the resulting EXAFS contribution is identical to a case where each Fe is surrounded by 3 Fe. More generally, the simultaneous presence of "heavy" (Me = Ti, V, Cr, Mn, Fe, Co, Ni...) and "light" (Mg, Al) atoms around the central atom results in destructive interferences, which reduce the wave amplitude in reciprocal space and, accordingly, the magnitude of second RSF peaks of phyllosilicates. Manceau (1990) first recognized this problem and recommended that in studies of the distribution of cations in the octahedral sheet of layer silicates, differentiation of the di- or trioctahedral nature of layer silicates be accomplished by alternative methods in combination with EXAFS. This question can be sensibly addressed in P-EXAFS by examining atomic pair correlations in the 3.5-6.5Å distance range.

In conclusion, the second RSF peak of natural clays obtained at the K-edge of the octahedral metal cation (Me) generally contains three predominant atomic pair contributions : Me-Tet_1, Me-$(Mg,Al)_1$, and Me-Me_1. The two next-nearest oxygen atoms (O_2 shell) near 3.4-3.5 Å (Table 1) have a negligible contribution, but not the group of 6 oxygens from the third shell (O_3) at ~3.7-3.8 Å, which gives a small contribution on the right tail of the second RSF peak (Manceau et al. 1998). This multi-shell contribution complicates spectral interpretation, and leads to a multiplicity of mathematical solutions whenever the total number of Tet_1 (2 or 4) and Oct_1 (3 or 6) cations are not fixed, and when individual Debye-Waller factors (σ) are not constrained to realistic physical values (typically 0.08 Å in clay structures) during least squares spectral fitting procedures (Manceau and Decarreau 1988). Under such fitting conditions, the numbers of Me-$(Mg,Al)_1$ and Me-Me_1 pairs calculated by spectral simulations are meaningful, and these values can be used to determine the statistical distribution of heavy and light cations in the octahedral sheet of clays with good accuracy owing to the π phase contrast between these two groups of atoms (Drits et al. 1997a; Manceau et al. 1990; Manceau and Calas 1986; Muller et al. 1997). It will be shown below that the accuracy of this analysis is even better in P-EXAFS experiments.

In the plane wave approximation, the theoretical expression that governs the angular dependence of EXAFS spectra in linearly polarized experiments is given by:

$$\chi_{ij}(k,\theta) = 3 < \cos^2\theta_{ij} > \chi_{ij}^{iso}(k) = \sum_{j=1}^{N_{cryst}} (3\cos^2\theta_{ij})\, \chi_{ij}^{iso}(k) \qquad [1]$$

where ij denotes the atomic pair under consideration, θ_{ij} is the angle between the electric field vector **E** and the vector $\mathbf{R}_{ij}$ that connects the absorbing i atom to the backscattering j atom, and $\chi_{ij}^{iso}(k)$ is the isotropic contribution of the j shell (Figure 3a). The summation is made over all the N_{cryst} atoms of the j^{th} shell, because for a given orientation of **E** with respect to the crystal, these atoms may not have the same θ angle. In a true powder (i.e. perfectly randomly oriented crystallites), θ takes all possible values in the space, and the $3\cos^2\theta$ term averages to 1 since

$$3 < \cos^2\theta_{ij} > = \int_0^{2\pi}\int_0^{\pi} 3\cos^2\theta \sin\theta\, d\theta\, d\Omega \Big/ \int_0^{2\pi}\int_0^{\pi} \sin\theta\, d\theta\, d\Omega$$

$$= \frac{1}{4\pi}\int_0^{2\pi}\int_0^{\pi} 3\cos^2\theta \sin\theta\, d\theta\, d\Omega = 1 \qquad (2)$$

It follows from equation (1) that neighboring j atoms located along the polarization direction (θ = 0°) are preferentially probed while atoms located in a plane perpendicular to **E** (θ = 90°) are not observed. Therefore P-EXAFS measurements provide orientation-dependent structural information, and can be used to probe the local structure of layer minerals between two different directional limits, parallel and perpendicular to the (001) plane, by varying the angle between **E** and the layer plane of a single crystal, or a film surface of a self-supporting film.

In a film preparation, typically the a and b axes of individual crystallites are randomly distributed around the normal to the film plane and, consequently, θ_{ij} varies from one crystallite to another. Thus, formula (1) cannot be easily handled, and requires transformation through the introduction of angles independent of the orientation of individual layers within the film plane. Because of the cylindrical, or fiber-like, symmetry of self-supporting films (see the texture section), the azimuthal Ω angle of $\mathbf{R}_{ij}$

(Figure 3a) varies from 0 to 2π if one wants to consider all crystallites, and can thus be be integrated over this angular range. Under this condition Eq. 1 can be transformed to (Manceau et al. 1998)

$$\langle\cos^2\theta\rangle = \cos^2\beta \sin^2\alpha + (\sin^2\beta\cos^2\alpha)/2 \quad (3)$$

where α is the angle between **E** and the film surface (i.e. the experimental angle), and β the angle between $\mathbf{R_{ij}}$ and the film normal (polar angle, Figure 3a). This polarization

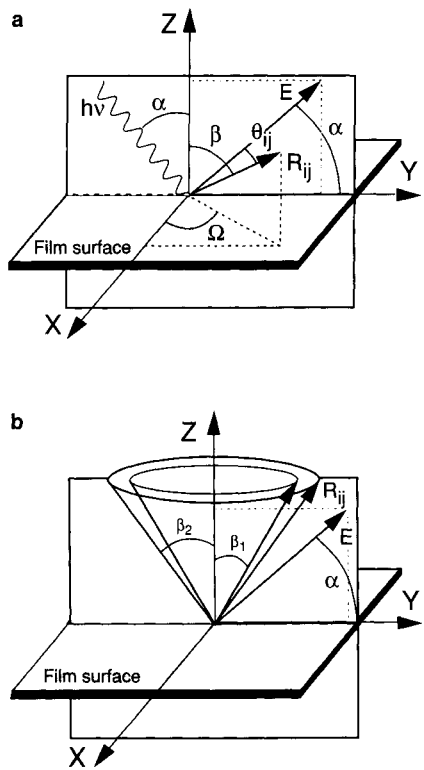

Figure 3. a) Coordinate system applicable to angular measurements on self-supporting films. XY is the film plane, and X-rays are incident on the YZ plane. α is the incidence angle between **E** and **Y**, β is the polar angle, and Ω the azimuthal angle of the atomic pair ij. θ_j is the angle between **E** and the atomic pair. b) Distribution of orientation of β angles of atomic pairs resulting from the misalignment of c* axis of individual particles perpendicularly to the film surface. The disorientation is equal to $\Delta\beta = \beta_2 - \beta_1$.

term is now independent of the relative position of crystallites in the film plane, and also of the variation of θ_{ij} from one atom to another in the j^{th} shell.

The amplitude of χ_{ij}^{iso} (k) is obviously proportional to N_{cryst}, but in a polarized experiment one detects an apparent number of neighbors, which is the effective number (N_{eff}) of atoms really seen at a given angle of α. Then:

$$\chi_{ij}(k,\alpha) = \frac{N_{eff}}{N_{cryst}} \chi_{ij}^{iso}(k) \quad (4)$$

with

$$N_{eff} = 3\, N_{cryst} [\cos^2\beta \sin^2\alpha + (\sin^2\beta \cos^2\alpha)/2] \quad (5)$$

In the normal ($\alpha = 90°$) and parallel ($\alpha = 0°$) orientation of the electric field vector, equation (4) reduces to

$$N_{eff}^{\parallel} = \frac{3}{2} N_{cryst} \sin^2\beta \quad (6)$$

$$N_{eff}^{\perp} = 3N_{cryst} \cos^2\beta \quad (7)$$

Thus, from the knowledge of the crystallographic β angle of a j^{th} shell it is possible to calculate the effective number of neighbors seen in a P-EXAFS experiment for the two independent orientations. Conversely, β in an unknown structure can be deduced from N_{eff} determined from the simulation of P-EXAFS spectra. From Eq. 5, when $\beta = 54.7°$ or $\alpha = 35.3°$, $N_{eff} = N_{cryst}$, which means that the atomic pair has no polarization dependence in the X-ray beam. The amplitude is thus constant and equal to that of a powder ($\chi_{ij}(k,\alpha) = \chi_{ij}^{iso}(k)$) whatever α. Thus, $\beta = 54.7°$ is a magic angle in the same manner as is $\alpha = 35.3°$. For $\beta < 54.7°$, $\chi_{ij}(k,\alpha)$ increases with α, whereas for $\beta > 54.7°$, $\chi_{ij}(k,\alpha)$ decreases with increasing α.

It will be shown now how these theoretical considerations apply to a clay structure taking Garfield nontronite as an example (Manceau et al. 1998). Interatomic

distances (R), β angles, N_{cryst}, $N_{eff}^{\parallel}$, and $N_{eff}^{\perp}$ for the successive atomic shells located at increasing distance from Fe atoms are listed in Table 2. Examination of Figure 4 and Table 1 and 2 shows that, in the context of phyllosilicates, P-EXAFS has the advantage of preferentially canceling the contribution from Fe-Oct_1 pairs ($N_{eff}^{\perp}$(Fe-(Fe,Al,Mg)$_1$) = 0) while simultaneously selecting Fe-Tet_1 pair contributions ($N_{eff}^{\perp}$(Fe-(Si,Al)$_1$) = 8.6) in the normal orientation. Conversely, when the polarization vector is parallel to the film plane, the Fe-Oct_1 contribution is preferentially reinforced ($N_{eff}^{\parallel}$=4.5), and the Fe-Tet_1 pair contribution becomes small ($N_{eff}^{\parallel}$=1.7). Thus, the residual Fe-Tet_1 contribution at α = 0° equals 1.7 / 8.6 = 20% of its amplitude at α = 90° and, therefore, the Fe-Oct_1 pair contribution can be isolated from the in-plane EXAFS spectrum by subtracting the residual out-of-plane Fe-Tet_1 component. This differential filtering of the Fe-Oct_1 and Fe-Tet_1 contributions in P-EXAFS experiments enhances the precision on N_{Oct1}. Additionally, in the parallel orientation the total wave amplitude of $\chi_{Fe\text{-}Oct1}(k)$ is enhanced by 50% as compared to $\chi^{iso}_{Fe-Oct1}$ because N_{eff} = 1.5 N_{cryst} (Eq. 6). This magnification of the electronic wave amplitude, completed by the filtering of the Fe-Tet_1 pair contribution as described above, increases the sensitivity of EXAFS as a tool to study the distribution of Oct-Oct and Oct-(Al,Mg) pairs in the octahedral sheet of layer silicates.

Table 2. Angular dependence of atomic shell contributions for Garfield nontronite in polarized EXAFS. After Manceau et al. (1998).

	R (Å)	<β>	N_{cryst}	$N_{eff}^{\parallel}$	$N_{eff}^{\perp}$
O_1	1.97-2.04	57°	6	6.3	5.3
Fe_1	3.05	90°	3	4.5	0
$(Si,Al)_1$	3.26	32°	4	1.7	8.6
O_2	3.45	11°	2	0.1	5.8
O_3	3.74-3.82	73°	6	8.2	1.5
O_4	4.03-4.21	37°	4	2.2	7.6
$(Si,Al)_2$	4.49	52°	4	3.7	4.5
Fe_2	5.28	90°	6	9	0
Fe_3	6.10	90°	3	4.5	0

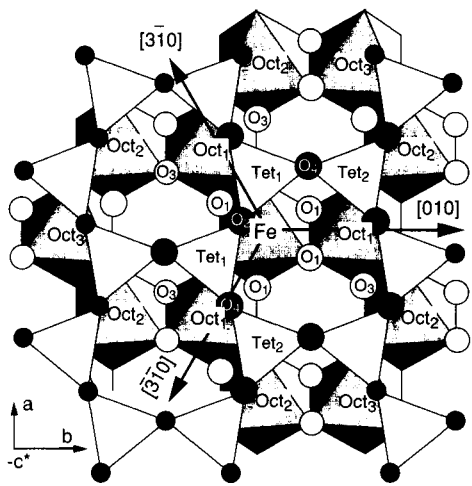

Figure 4. Projection down c* of a dioctahedral layer silicate (one tetrahedral sheet is not shown), and representation of the successive atomic shells around a central Fe atom. Blank triangles are (Si,Al)O_4 tetrahedra (Tet), black atoms are basal oxygens, blank atoms are oxygens from the octahedral sheet, and grey atoms are OH groups. Oct denotes either Fe, Al, or Mg.

Eqs. 4 to 7 assume that individual platelets have their (001) basal surface perfectly parallel to the film plane. If dispersion from this orientation occurs, N determined from experimental P-EXAFS spectra (N_{exafs}) would be intermediate between N_{eff} and N_{cryst} leading to a diminution of the polarization dependence of the amplitude. This reduction can be easily calculated in the case of a *homogeneous* distribution of the tilt angles of atomic pairs around their average β value. N_{exafs} is obtained from Eq. 2 by integration over a range $0 \leq \beta_1 \leq \beta \leq \beta_2$ where β_1 and β_2 denote the minimum and maximum polar tilt angles of β due to the misalignment of particles in the film (Figure 3b) (Stöhr and Jaeger 1982).

$$N_{exafs} = N_{cryst} \int_0^{2\pi} \int_{\beta 1}^{\beta 2} 3\cos^2\theta \sin\theta d\theta d\Omega \Big/ \int_0^{2\pi} \int_{\beta 1}^{\beta 2} \sin\theta d\theta d\Omega \quad (8)$$

which reduces to

$$N_{exafs} = N_{cryst}\left[1+\frac{1}{2}(3\sin^2\alpha - 1)\left(\frac{\cos^3\beta_1 - \cos^3\beta_2}{\cos\beta_1 - \cos\beta_2} - 1\right)\right] \quad (9)$$

The influence of this disorientation on the polarization dependence of EXAFS spectra was calculated for $\Delta\beta = \beta_2 - \beta_1 = 20°$ and 40°. Results are reported in Figure 5 in the form of N_{exafs} / N_{cryst} as a function of α. Since $\alpha = 35.3°$ and $\beta = 54.7°$ are magic angles, $N_{exafs} = N_{cryst}$ for all β and $\Delta\beta$ values when $\alpha = 35.3°$, as well as all α values when $\beta = 54.7°$. In the absence of disorientation, this figure shows that in-plane atomic pairs are magnified by 1.5 in the parallel orientation ($N^{\parallel}_{exafs} / N_{cryst} = 1.5$ for $\beta = 90°$ and $\alpha=0°$), and out-of-plane atomic pairs are enhanced by 3.0 in the perpendicular orientation ($N^{\perp}_{exafs}/N_{cryst} = 3$ for $\beta = 0°$ and $\alpha=90°$), which is in agreement with Eqs. 6 and 7.

The reduction of the polarization dependence is negligible for a disorientation of the particles within the film plane of $\Delta\beta/2 = 10°$ (Fig 5a), but is observable when $\Delta\beta/2 = 20°$ (Fig 5b). The magnitude of this reduction varies with both β and α, and the function $\Delta(N_{exafs}/N_{cryst})_{0\text{-}20°}=f(\alpha,\beta)$ for $\Delta\beta/2 = 20°$ is plotted in Figure 5c. We see that the difference between the number of atomic neighbors (N_{cryst}) and the amount detected by EXAFS is maximum for $\beta = 10°$ regardless of α, and is always greater in the perpendicular than in the parallel orientation for a given β value. *An important conclusion is that the perpendicular orientation is much more sensitive to an imperfect film texture than the parallel orientation, and that atomic pairs which are inclined by 10 to 30° with respect to c* have, as a result, a diminished amplitude compared to other inclinations.* For instance, in the case of phyllosilicates $\beta_{Si1}=32°$ so that $\Delta(N_{exafs}/N_{cryst})_{0\text{-}20} = -0.22$ for $\alpha = 90°$, and since $N_{cryst} = 4$ (Table 2), then $N^{\perp}_{Si1}$ is reduced from 8.6 (Table 2) to 7.7 ($\Delta N = 0.9$). Likewise, $\Delta(N_{exafs}/N_{cryst})_{0\text{-}20} = 0.11$ for $\alpha = 0°$ and, consequently, $N^{\parallel}_{Si1}$ is increased from 1.7 (Table 2) to 1.7+(0.11x4)=2.1 ($\Delta N = 0.4$) when $\Delta\beta/2 = 20°$. The *relative* variation of N, which is equal to $(N_{eff} - N_{exafs}) / N_{eff}$, is about 10% at $\alpha = 90°$ ((8.6-7.7)/8.6=0.11) and 23% at $\alpha = 0°$. Concerning the Oct_1 shell, $\Delta(N_{exafs}/N_{cryst})_{0\text{-}20} = 0.12$ for

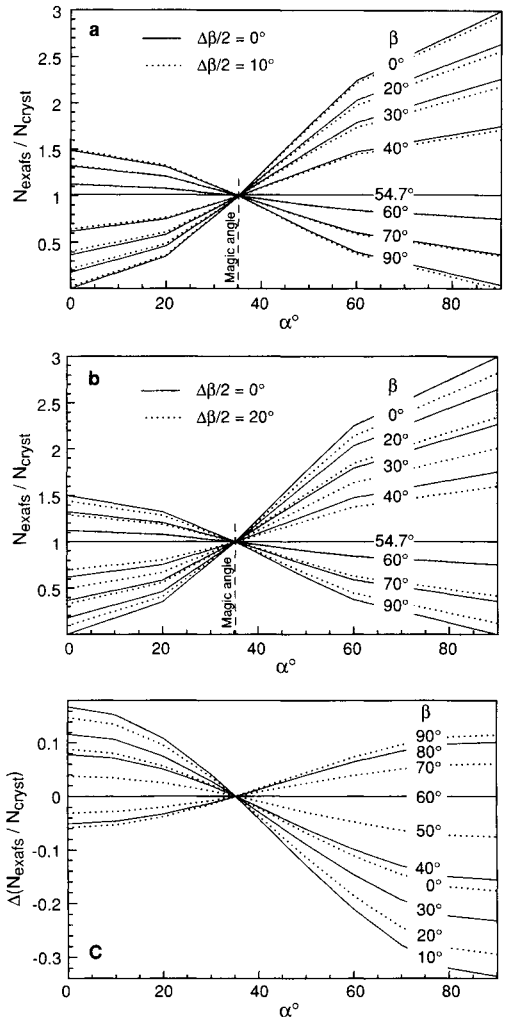

Figure 5. a-b) Plot of N_{exafs} / N_{cryst} (dotted lines) as a function of the experimental α angle for different β angles and for $\Delta\beta = 0°$ ($N_{exafs} = N_{eff}$, solid lines), 10° and 20° (dotted lines). c) $\Delta(N_{exafs}/N_{cryst})=f(\alpha,\beta)$ function for $\Delta\beta/2 = 20°$. The difference between the real number of atomic neighbors (N_{cryst}) and the amount detected by EXAFS (N_{exafs}) is maximum for $\beta = 10°$ regardless of α.

α = 90°, thus $N^{\perp}_{Fe1}$ equals 0.12x3=0.36 in dioctahedral structures, and 0.12x6=0.72 in trioctahedral structures instead of 0 (ΔN = 0.4 and 0.7), which corresponds to a relative variation of 0.36 / 3 = 12%. At α = 0° the difference between N_{eff} and N_{exafs} for the Oct_1 shell is as low as 4%. These values are within the range of precision on N classically obtained from the least-squares fitting of EXAFS data (typically 10 to 20 %). Consequently, self-supporting films in which the misalignment of particles is lower than ~ ± 20° can be treated, in a first approximation, as single crystals having a 3-fold or higher symmetry axis (Manceau et al. 1998). One important consideration, however, is that due to incomplete theoretical treatment, our calculations are only a first step and assume a linear distribution of orientations from β_1 to β_2, when in fact texture goniometry reveals that this distribution is Gaussian. While further theoretical treatments should endeavour to incorporate the Gaussian orientation distribution of bond vectors, only the magnitude of N_{exafs}/N_{cryst}° and $\Delta(N_{exafs}/N_{cryst})_{0\text{-}20}$ should be affected. We suspect that the overall trends in orientation distribution will remain unchanged.

METHODOLOGY

Obtaining the Out-of-plane EXAFS Spectrum

P-EXAFS spectrum in the parallel orientation $\chi_{i\ j}(k,\alpha=0°)$ can be readily obtained by placing the film normal to the beam direction (Figure 6a). EXAFS spectra of concentrated samples are measured in transmission mode on thin preparations of typically 10 to 100 μm. For films, $\chi(k,\alpha=90°)$ is not experimentally measurable, but a theoretical spectrum can be obtained from a linear regression analysis of angular measurements at $0° \le \alpha \le 60°$ as χ varies as $\cos^2\alpha$ (Brouder 1990; Heald and Stern 1977; Manceau et al. 1988). The theoretical expectation is confirmed by the plot in Figure 6b. The linearization procedure is particularly reliable because $\cos^2 0° = 1$ and $\cos^2 60° = 1/4$, which means that 75% of the variation range of this function is accessible by direct measurement. Therefore extrapolation is minimized. Also, since $\chi(k,\alpha=90°)$ is mathematically obtained following measurement of several spectra, statistical noise is reduced and experimental errors of individual measurements are minimized. The accuracy of the extrapolation can be assessed by comparing an experimental spectrum to that recalculated from the regression analysis at a particular experimental angle. On a Garfield nontronite film, Manceau et al. (1998) showed that the two spectra were nearly identical.

EXAFS spectra of more dilute samples are measured in fluorescence mode with the detector placed parallel to **E**. In this case, $\chi(k,\alpha=90°)$ can still be calculated by the previous procedure, but can also be obtained experimentally by tilting the sample to grazing incidence and by collimating or focussing the beam on the sample (Figure 6b). This geometry cannot be adopted on all spectrometers as it requires a high brightness source for collimation or a focused beam to preserve a high density of photons on the diluted sample. In these situations it is possible to reach a grazing incidence of ~10°, and thus to collect directly $\chi(k,\alpha=80°)$, which is generally assumed to be identical to $\chi(k,\alpha=90°)$. At this angle the error on $\cos^2\alpha$ is only 3%, and is acceptable in regards to the orientation distribution of individual crystallites off the film normal, which is at best ~ 10° of half width at half maximum (see next section).

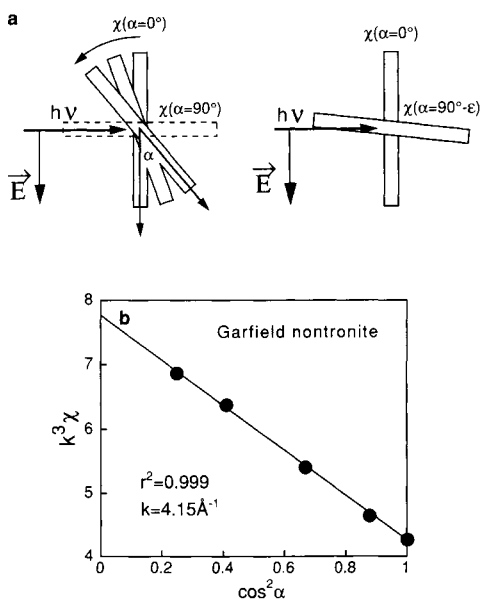

Figure 6. a) Measurement of angular spectra in transmission mode (left) and grazing incidence (right). In both cases, the film is rotated around an axis perpendicular to both the beam direction and **E**. b) Plot of $k^3\chi$ as a function of $\cos^2\alpha$ which confirms the expected angular dependence of EXAFS spectra.

Texture of Self-supporting Films

Application of P-EXAFS to fine-grained layer minerals requires samples with a high degree of preferred orientation of the constituent crystallites in order to accurately

locate scattering atoms relative to the polarization direction. In polycrystalline films, *ab* crystallographic planes of individual platelets are preferentially aligned parallel to the film surface, but important deviations from this orientation may occur. This distribution, in most cases for self-supporting films, adopts a Gaussian shape. Obviously, the stronger the in-plane alignment, the larger the resulting angular anisotropy of P-EXAFS spectra, and it is important to know the true misalignment of particles for the quantitative analysis of P-EXAFS spectra because equation (5) necessarily assumes a perfect orientation.

Self-supporting films also differ from single crystals by the orientation of crystallites within the film plane. The *a* and *b* axes of crystallites are *a priori* randomly oriented around the normal to the film plane, and the film is expected to exhibit a cylindrical axis of symmetry perpendicular to the film plane. However, this assumption requires verification at least once for each of the different families of layered compounds investigated by P-EXAFS because equation (2) is derived from (1) by averaging the azimuth angular dependence of $\mathbf{R}_{ij}$, i.e. by assuming a C_∞ axis about the film normal.

These considerations lead to the conclusion that accurate determination of the orientation distribution (OD) of crystallites in the film is necessary to quantitatively interpret P-EXAFS spectra. The OD is generally measured by diffraction (with X-rays in our case) using a four-circle diffractometer (Schulz 1949; Wenk 1985). The experiments involve measuring the so-called {hkl} pole figures, relative to the specific {hkl} equivalent crystallographic planes of the material. The diffractometer has three rotation movements : the Bragg angle (θ_{hkl}), the azimuth (φ), and colatitude (ρ) rotations (Figure 7a). After having fixed θ_{hkl} for the sample (and $2\theta_{hkl}$ for the detector) so as to obtain diffraction from the {hkl} planes, all crystallites are brought successively into a diffraction position by rotating the sample around ρ and φ. For each (ρ,φ) position the diffracted intensity, $I_{hkl}(\rho\varphi)$, is proportional to the number of {hkl} planes which are in the $(-\rho,-\varphi)$ orientation in the sample. Figure 7b illustrates, by looking down on Figure 7a, how individual crystallite planes of orientation $(-\rho,0)$ are brought into a diffraction position by a ρ rotation. In this figure, only the black {hkl} planes diffract for the given θ_{hkl} angle.

Once diffracted intensities have been measured for all possible (ρ,φ) positions, they are projected onto the sample plane using an equal-area projection for qualitative visual representation and subsequent quantitative analysis of the textural order of the

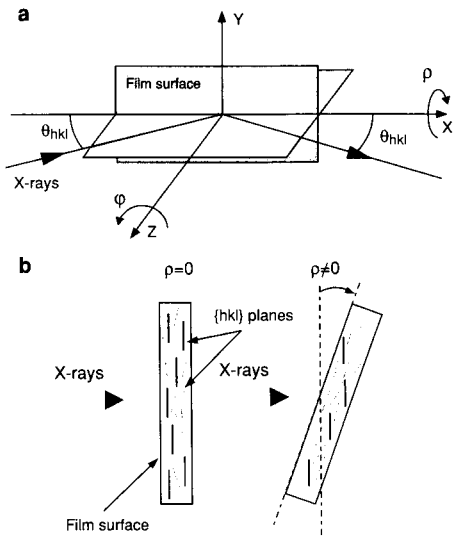

Figure 7. X-ray diffraction reflection geometry used for texture analysis. a): A {hkl} pole figure is measured for a fixed θ_{hkl}, while the sample is rotated by ρ and φ (both conserving θ_{hkl}). b): Side view of (a) showing how individual crystallographic planes within the film are brought to a diffraction position by a rotation of ρ.

sample. Imagine an extreme case of a sample composed of one single crystal aligned with its main crystallographic axes [100], [010], and [001], respectively, parallel to the macroscopic XYZ reference frame (Figure 8a, left). The corresponding theoretical {001} pole figure (right) consists of restricted high intensity regions where the normals to the (001), (100) and (010) crystallographic planes ([001]*, [100]*, and [010]*, respectively) are located. The normal to the slab corresponds to the [001] direction of the crystal, and is in the center of the pole figure (parallel to the Z axis), which indicates that *ab* planes of the crystal are parallel to the XY slab plane. The other [100] and [010] directions are parallel to X and Y respectively. An inclined direction, [111] for instance (Figure 8b), would be represented by a pole at ρ = 55.35° and φ = 45° (for a cubic crystal system) in the pole figure frame. These two pole figures could have been obtained on a polycrystalline sample with all crystallites perfectly aligned as previously. On the other hand, for a sample having its [100] and [010] directions randomly distributed around the Z axis (axisymmetric texture, Figure 8c), one would obtain rings of high diffracted intensities at the corresponding ρ angles.

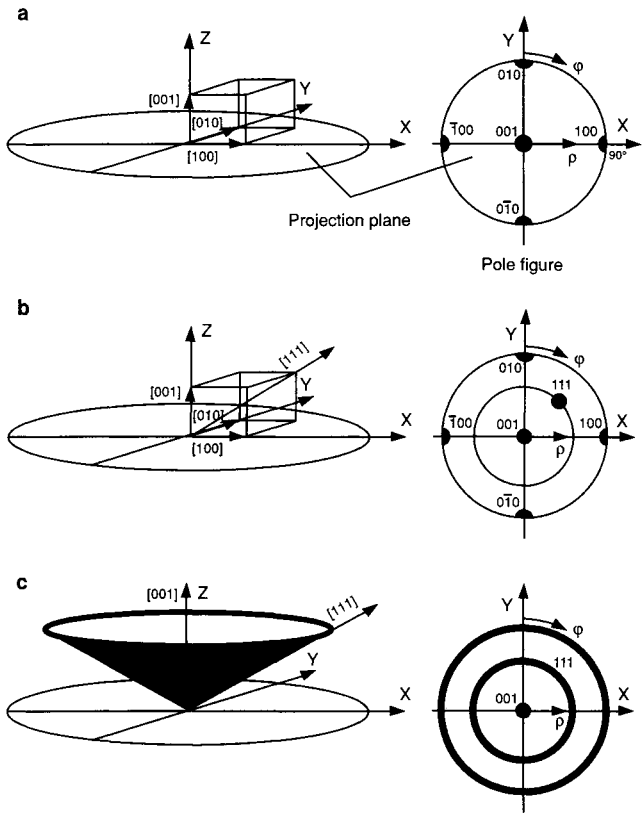

Figure 8. a) Definition of the projection plane for a pole figure, with respect to sample coordinates (left) and schematic {001} pole figure in the case of a single crystal with cubic symmetry with main axes oriented parallel to the sample frame (right). b) [111] crystalline direction for the single crystal (left) and its localization on the pole figure frame (right), not shown here are the other equivalent crystal directions for a cubic crystal symmetry. c) Same as in b) for a set of crystals randomly oriented around Z with [001] directions parallel to Z (<001> fiber texture), the pole figure exhibits rings for all directions at the corresponding ρ value.

In order to compare the texture strength of different samples independently from their porosity or from the presence of ancillary phases, etc., it is necessary to normalize the diffracted intensities into $P_{hkl}(\rho,\varphi)$ pole densities. Pole densities are

expressed in mrd, or ***multiple of a random distribution***, and are equal to 1 mrd for a random sample whatever hkl and (ρ,φ), while pole figures of oriented samples will exhibit values above and below 1 mrd. In layered minerals, only a few hkl reflections are accessible to the experiment because of poor (or lack of) 3D periodicity, high d-spacings (θ_{hkl} is often too low to ensure constant sample irradiation), and systematic extinctions. These limitations prevent the measurement of a sufficient number of pole figures to ensure that all texture components are revealed, though information on all components is present in all pole figures. The measured diffraction peaks generally derive from several overlapping reflections, which result in ***multipole*** figures of complex direct interpretation. It is then absolutely necessary to calculate the complete OD from these multipole figures to obtain a quantitative description of the texture. Once the OD is determined, every desired non-overlapping ***single pole*** figure can be recalculated. The OD is generally refined by an iterative method, which minimizes the reliability factors, RP:

$$\overline{RP} = \frac{1}{I}\sum_{hkl}\sum_{\rho\varphi}\frac{P_{hkl}^{calc}(\rho\varphi) - P_{hkl}^{obs}(\rho\varphi)}{P_{hkl}^{obs}(\rho\varphi)} \qquad (10)$$

where P^{obs} and P^{cal} refer to the observed and recalculated normalized intensities of pole figures. RP factors depend on the texture strength and, consequently, make comparison of the quality of the refinement between samples somewhat ambiguous. This drawback can be eliminated by introducing weights (w), which incorporate the regular statistical distribution of the measured (obs) and recalculated (calc) diffracted intensities $I_{hkl}(\rho\varphi)$.

$$\overline{Rw}^{2} = \frac{1}{I}\sum_{hkl}\sum_{\rho\varphi}\frac{\left[w_{hkl}^{obs}\ I_{hkl}^{obs}(\rho\varphi) - w_{hkl}^{calc}\ I_{hkl}^{calc}(\rho\varphi)\right]^{2}}{w_{hkl}^{calc\,2}\ I_{hkl}^{calc\,2}(\rho\varphi)} \qquad (11)$$

The overall texture strength is quantified with the texture index F^2 (Bunge 1981)

$$F^2 = \frac{1}{8\pi^2}\sum_{g}\left[f(g)\right]^2\Delta g \qquad (12)$$

where f(g) is the orientation distribution function representing the orientation distribution of the constituent crystallites, and Δg is the OD cell volume.

It will be shown in the next section that with smectitic clays it is possible to prepare self-supporting films in which the crystallite dispersion has a half width at half maximum (HWHM) of ~10°. In this condition, the dispersion of c^* axis around the film normal can be neglected and $N_{EXAFS} \approx N_{eff}$ as shown in the EXAFS section.

APPLICATIONS

Dioctahedral Clay Structures

Experimental-normalized and OD-recalculated multipole figures for Garfield nontronite are presented in Figure 9a. OD-recalculated patterns look very similar to those obtained experimentally, and provide an assessment of the reliability of the texture calculation. The {113} and {11$\bar{3}$} reflections of the {004/113/11$\bar{3}$} overlap appear as a maximum on a ring at about ρ = 42°, highlighted by a dashed circle. This value is consistent with the crystallographic structure of nontronite since the angle between (004) and (113) equals 38.7°, and the angle between (004) and (11$\bar{3}$) equals 46°. The texture index F^2 is as high as 60.9 mrd^2, and the reliability factors RP_1 and Rw_1 (for density values above 1 mrd) are equal to 10.8% and 5.8%, and RP_0 and Rw_0 (for all densities) to 17.8% and 8.1%. Rw weighted factors are lower than RP because they are less dependent on F^2. The relatively higher values obtained for R_0 compared to R_1 are explained by the poorer diffraction to background ratio of the oblique reflections. All these values are fairly low, and compare favorably with recent results obtained on compounds having a similar texture strength (Chateigner et al. 1997; Wenk et al. 1996).

The {020/110} and {200/130} multipole figures form regular rings of iso intensities, which means that *a* and *b* axes are randomly distributed in the sample plane. Note that the orientation distribution of *a* and *b* axes can only be determined from oblique reflections because {00*l*} pole figures have obviously no sensitivity to the orientation of crystallites in the perpendicular [100] and [010] directions. This result indicates that the distribution of crystallites is axisymmetric with the symmetry axis parallel to the film normal. This texture is called a '<001>* fiber texture'. The pole figures lack any other textural component, and as such the assumption made in generating Eq. 3 applies to self supporting films of layered minerals.

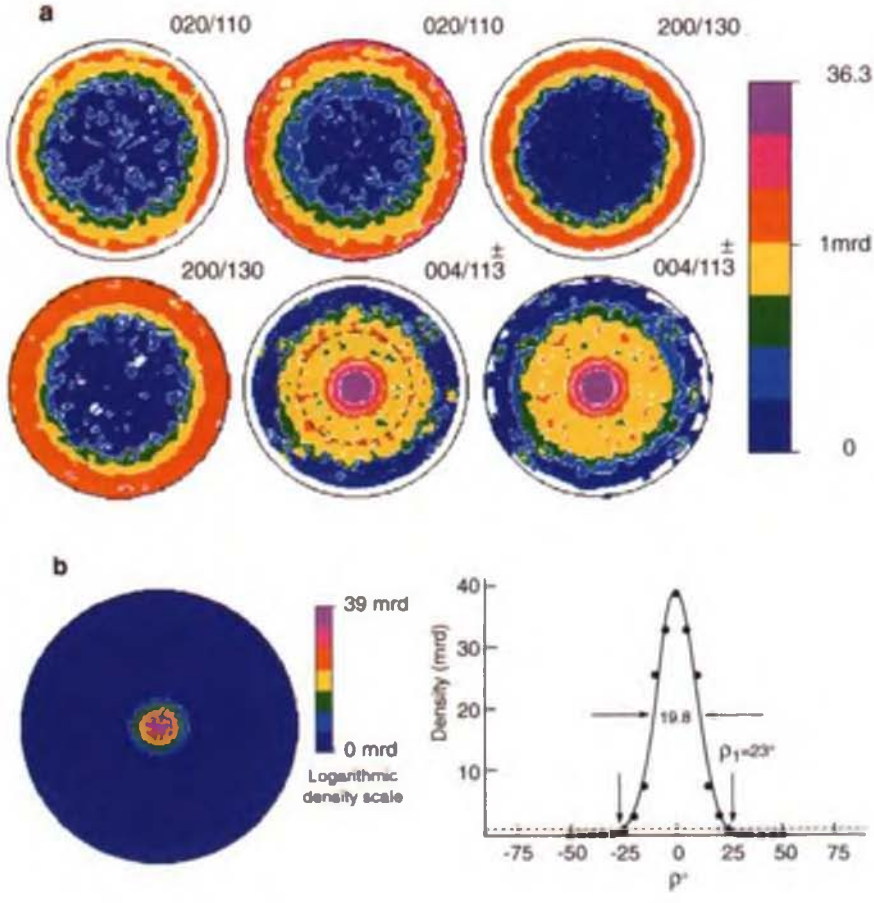

Figure 9. a) Experimental normalized and OD-recalculated pole figures (upper left to lower right in successive order) for Garfield nontronite. Experimental pole figures are satisfactorily reproduced by the computation. The dashed circle on the $\{004/\overline{1}\,1\overline{3}\}$ pole figure represents the $\{1\overline{1}3\}$ trace. Due to the turbostratic structure of smectites this latter reflection has a very low intensity on the powder XRD pattern of nontronite, and appears as a scattering background in the prolongation of the 020 reflection. In {020/110} and {200/130} pole figures, zones of iso densities form regular rings, which indicates that the film possesses a <001>* fiber texture. The intensity of $\{1\overline{1}3\}$ in the $\{004/\overline{1}\,1\overline{3}\}$ pole figure is 15%.

b) Non overlapped {001} recalculated pole figure and integrated ρ scan of the previous pole figure showing the angular dispersion of c* for the individual crystallites. The 1 mrd density level is represented by an horizontal dashed line.

The {004/113/11$\bar{3}$} multipole figure does not reveal the maximum density of the OD since it corresponds to an overlap of reflections, nor does it allow for a clear visualization of crystallite dispersion within the film since individual reflections of the overlap are not located at exactly the same ρ angle. The {001} single pole figure was thus calculated from the OD (Figure 9b, left). A comparison of Figure 9a and 9b shows that the central spot is smaller for the single {001} pole than for the {004/113/11$\bar{3}$} pole figure as a result of the overlap deconvolution. The maximum orientation density reaches 39 mrd. To our knowledge, this is the first report of such a high texture for monoclinic self-supporting films. Since the film has a fiber-like texture, the full distribution density can be simply represented by a radial section of the pole figure (Figure 9b, right). The ρ scan of Figure 9b has been obtained by averaging the {001} densities over all φ angles for each ρ value. Examination of this figure shows that the maximum dispersion of c* axis is ~26°, as beyond this value the orientation density vanishes. The full width at half maximum of the crystallite dispersion is equal to 19.8°, and ρ_1 at the 1 mrd density level is 23°. We can thus consider that the out-of-plane distribution of the *c** axis for individual crystallites within the film is negligible (~10°) and, consequently, the difference between N_{eff} estimated from the crystallographic structure assuming an ideal texture, and its real value experienced by P-EXAFS, N_{exafs}, can be ignored.

k^3-weighted P-EXAFS spectra recorded in transmission mode for the Garfield nontronite film are shown in Figure 10. The 90° spectrum has been calculated using the linear regression method described in the methodology section. Of particular importance in these spectra are isosbestic points where χ(k) is independent of α. The presence of these points indicates a high homogeneity in sample thickness and provides good evidence that differences observed in the spectra are due to orientation effects alone. Additionally, the large dependence upon polarization in regions between isosbestic points is consistent with the successful preparation of a highly oriented clay film. Accordingly, the observed changes in amplitude can be safely interpreted in terms of structural properties.

Radial structure functions (RSFs) obtained by Fourier transforming k^3-and k-weighted P-EXAFS spectra are shown in Figure 11a and 11b. The structural nature of RSFs peaks was determined by *ab initio* FEFF calculations (Rehr et al. 1991) performed on a nontronite cluster modeled from valence-distance least squares methodologies (Manceau et al. 1998). Theoretical Fourier transforms obtained for α = 0° and 90° are contrasted to experimental data in Figure 12 The position, amplitude and phase

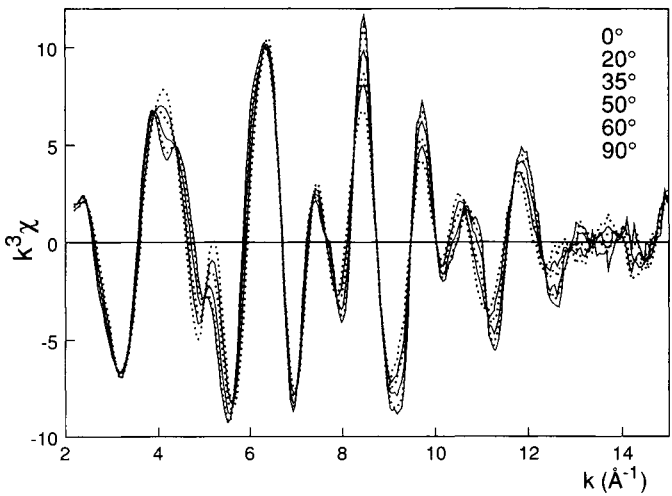

Figure 10. k^3-weighted Fe K-edge polarized EXAFS spectra for Garfield nontronite at α angles of 0°, 20°, 35°, 50° and 60°. The 90° spectrum has been obtained by regression of the experimental amplitude (see text). The amplitude of χ decreases with increasing α at 8.5 Å^{-1}, and increases with α at 4 Å^{-1}. Note the presence of isosbestic points where $\chi(k,\alpha)$ is independent of α.

(imaginary part) of all contributions are quantitatively reproduced to a high degree of accuracy for the two orientations up to ~ 6 Å. It is important to emphasize that this spectral match between *ab initio* simulations and experimental data was obtained with virtually no adjustment. Only Debye-Waller (σ) parameters were adjusted to values reported in the literature for clays (Manceau et al. 1988; Manceau et al. 1990; Manceau and Calas 1986; O'Day et al. 1994). This quantitative agreement indicates that P-EXAFS spectra are insensitive to a slight dispersion of the c^* axis of individual crystallites off the film plane and, consequently, that this film sample can be regarded as a single crystal for P-EXAFS experiments.

Peak A corresponds to the ligation O,OH shell (O_1, Figure 4), and the flattening angle (Bailey 1991) of the $Fe(O,OH)_6$ octahedron can be calculated from the angular dependence of its amplitude (Manceau et al. 1998). In the in-plane orientation, the contribution from Fe_1 atoms at the crystallographic R distance of R =

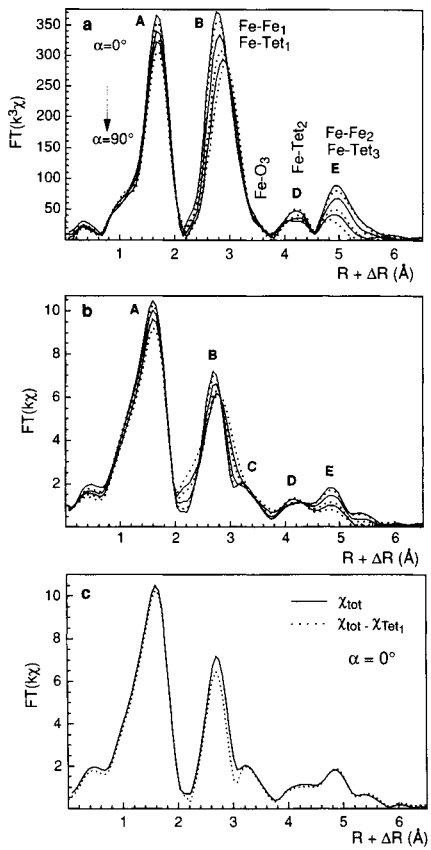

Figure 11. a)-b) k^3- and k-weighted Fe K-edge polarized RSFs for nontronites at α angles of 0°, 20°, 35°, 50°, 60°, and 90°. The amplitude of peaks A, B and E decreases with increasing α. c) Comparison of k-weighted RSF for Garfield nontronite at α = 0° to the same RSF obtained after subtraction of the Fe-Tet_1 contribution.

3.05 Å is enhanced ($N_{eff}^{\parallel} = \frac{3}{2} N_{cryst} \sin^2\beta = 4.5$), and peak B yields an apparent distance (i.e. not corrected from the phase shift function) of R + ΔR = 2.8 Å. In the out-of-plane orientation the contribution from the octahedral sheet is cancelled ($N_{eff}^{\perp} = 3N_{cryst}\cos^2\beta = 0$), and that of the Tet_1 shell at R ~ 3.26 Å is maximized ($N_{eff}^{\perp} = 3N_{cryst}\cos^2\beta = 8.6$, Table 2). Accordingly, peak B gradually shifts from R +

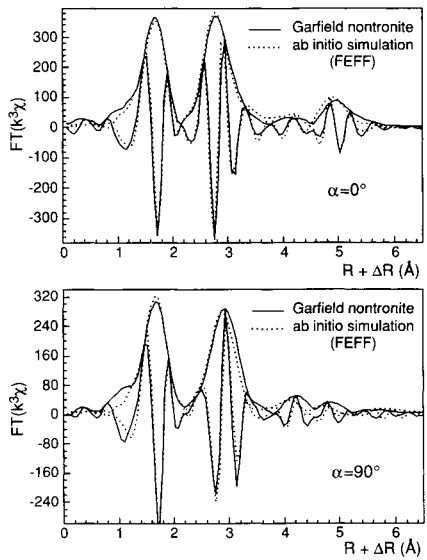

Figure 12. Comparison of experimental (solid line) and FEFF Fourier transforms (dotted line) of Fe K-edge EXAFS spectra for Garfield nontronite obtained at $\alpha = 0°$ and 90°.

3.05 Å is enhanced ($N_{eff}^{\parallel} = \frac{3}{2} N_{cryst} \sin^2\beta = 4.5$), and peak B yields an apparent distance (i.e. not corrected from the phase shift function) of R + ΔR = 2.8 Å. In the out-of-plane orientation the contribution from the octahedral sheet is cancelled ($N_{eff}^{\perp} = 3N_{cryst}\cos^2\beta = 0$), and that of the Tet_1 shell at R ~ 3.26 Å is maximized ($N_{eff}^{\perp} = 3N_{cryst}\cos^2\beta = 8.6$, Table 2). Accordingly, peak B gradually shifts from R + ΔR = 2.8 Å to 2.9 Å with increasing α. Peak D originates from the next-nearest tetrahedral shell (Tet_2), while peak E originates from both the next nearest octahedral shell (Oct_2) and third nearest tetrahedral shell (Tet_3) (Figure 4). Another peak, labeled C in Figure 11b, is observed for $\alpha = 0°$ when the Fourier transform is performed on $k\chi(k)$ instead of $k^3\chi(k)$. This peak corresponds to the O_3 shell (Table 2). Figure 11b compares the k-weighted RSF at $\alpha = 0°$ to that obtained after subtracting the residual Tet_1 component as explained in the theoretical section. Examination of Figure 11c clearly shows that the elimination of the tetrahedral contribution, combined with differential k-weighting, results in better resolution of the Fe-Oct_1 and Fe-O_3 components, simply because the Tet_1 shell lies at intermediate distance (Table 2). This analysis illustrates the improved spectral discrimination procured by angular measurements. Peak B in Figure 11c only

arises from the contribution of octahedral cations ($\chi_{Fe\text{-}Oct1}$), and least squares analysis permits calculation of N_{oct1} with an enhanced accuracy, thus improving the precision of the method for studying the statistical distribution of cations within the octahedral sheet of smectites of various elemental compositions (Manceau et al., 1999a).

Trioctahedral Clay Structures

In Figure 13 are contrasted the RSFs for a trioctahedral mica (#B13 in Manceau et al. 1990) and for the Garfield nontronite. Comparison of the amplitudes obviously shows lower A and B peaks in biotite compared to nontronite, despite the presence of 6 nearest octahedral cations in biotite vs 3 in nontronite (Figure 2b). This effect partly results from a difference of static disorder between the two phyllosilicates. The composition of this biotite sample is $(Si_{5.6}Al_{2.4})$ $(Fe^{3+}_{0.4}Fe^{2+}_{2.5}Al_{1.0}Mg_{1.1}Ti_{0.3}Mn_{0.2}Li_{0.2})$ $K_{\sim 2}O_{\sim 20}(OH, F)_{\sim 4}$ (Sanz et al. 1984), and the complex chemical composition of the octahedral sheet, as well as Fe^{3+} for Fe^{2+} substitutions, produce octahedral distortions. As a result, M1 and M2 sites are not regular and do not have similar dimensions. This distortion extends to nearest Fe-Oct distances, which were found to vary from 2.97 to 3.13 Å in the 1M biotite from Ruiz Peak, New Mexico (Takeda and Ross 1975). In nontronite, the Fe-Fe_1 distances are all equal to 3.05 Å, and the difference in coherency of the metal-metal distances between nontronite and biotite partly accounts for the different amplitudes observed for peak B. As explained previously, the mixing of Mg and Fe atoms in the nearest cation shell also decreases the amplitude of peak B in biotite owing to the phase contrast between Fe and Mg atoms.

Inspection of Figure 13a shows that the RSF for biotite exhibits three additional peaks, labeled F, G, and H, not observed for nontronite. These three peaks exhibit a very strong dichroic dependence: peaks G and H are observed at only 90° and 0°, respectively, and peak F is strongly diminished at $\alpha = 0°$. Peak G was identified by FEFF simulations as arising from the $(Si,Al)_3$ shell at 5.4 - 5.5 Å, and from interlayer K at 5.30Å ($\beta = 19°$, Takeda and Ross 1975). This peak is shifted to shorter distance in Na-nontronite (Figure 13b) as a result of the shorter Fe-Na distance (5.12Å). The intensity of this peak is decreased for at least four reasons: (i) Oct-$(Si,Al)_3$ distances are more incoherent in dioctahedral structures, (ii) Na is a weaker scatterer, (iii) Fe-Na and Fe-$(Si,Al)_3$ waves are nearly out of phase ($\Delta R \sim 0.3$Å), and (iv) the nontronite has a lower layer charge resulting in less interlayer Na involved in scattering processes. Unlike peak G, peaks F and H originate from atoms located within the layer framework, and are much more sensitive to the di-, trioctahedral character of the octahedral sheet.

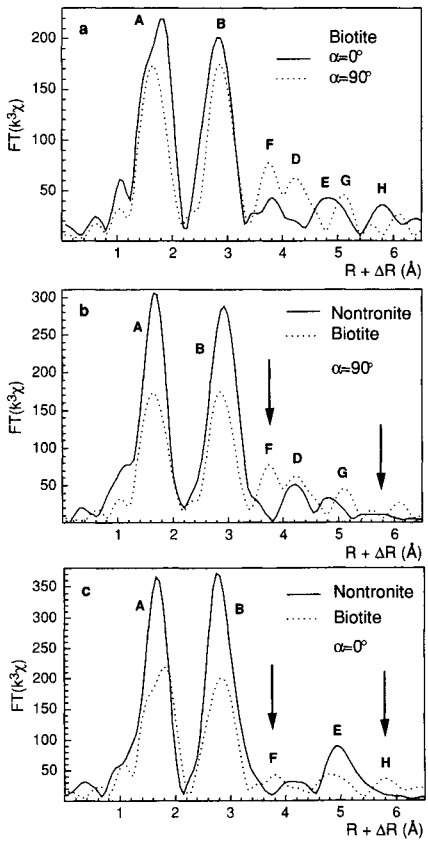

Figure 13. a) k^3-weighted RSF for biotite at $\alpha = 0°$ (full line) and 90° (dotted line). b-c) Comparison of k^3-weighted RSFs for Garfield nontronite (full line) and biotite (dotted line).

Peak F (Figure 13) corresponds to the contribution of the O_4 shell of the tetrahedral basal plane (Figure 4). As illustrated in Figure 14, basal oxygens are at the same z position in trioctahedral structures, and thus form an identical β angle of 37° in biotite (Takeda and Ross 1975). In addition, the Fe-O_4 distances are coherent in trioctahedral structures (≈ 4.15 - 4.20 Å), and these two factors enhance the contribution of basal oxygens in the out-of-plane orientation. In dioctahedral structures, the O_4 atoms undergo a vertical displacement to relieve the misfit between the octahedral sheet and the attached tetrahedral sheet (Lee and Guggenheim 1981). This corrugation of the oxygen basal plane modifies the β angle, and splits the Fe-O_4 distances causing the disappearance of peak F in the experimental RSFs of nontronite (e.g. in Garfield

nontronite d(Fe-O_4) = 4.03 - 4.21 Å, Table 2). This analysis infers that vacant octahedral sites can be indirectly detected by analyzing the out-of-plane structure of phyllosilicates. In our opinion, dioctahedral and trioctahedral layer silicates can be more reliably differentiated on the basis of this intrinsic structural criterion rather than by a curve fitting determination of the number of nearest neighbor Me-Me pairs as discussed in the first section of this chapter.

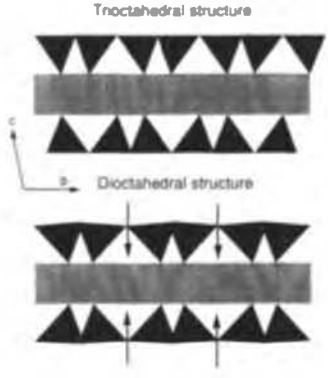

Figure 14. Representation of the biotite and nontronite structure projected down [100]. Trioctahedral structures have a flat basal plane, whereas dioctahedral structures are corrugated.

In the biotite RSF (Figure 13), peak H is located at twice the distance of peak B (R + ΔR = 5.8 Å), and thus corresponds to the third Fe shell (Fe_3) at R = 6.2 Å. It is interesting to note that the more distant Fe_3 shell has a similar amplitude as that of the Fe_2 shell at R = 5.3 Å (peak E, Figure 13a). Since the amplitude of the EXAFS signal decreases as 1 / R^2, the Fe_3 shell contribution would be expected to be diminished by 25%. In addition, interatomic distance calculations for biotite (Takeda and Ross 1975) shows that Fe - Fe_3 distances are much more incoherent (6.10 Å < R < 6.26 Å) than Fe - Fe_2 distances (R = 5.33 Å). Thus, the greater disorder of the third Fe shell also lessens the intensity of Fe_3 relative to Fe_2. Ab initio FEFF calculations showed that peak H is in fact amplified by a shadowing (focusing) multiple scattering (MS) effect between colinear octahedral cations (Manceau et al. 1998; O'Day et al. 1994). The MS effect between outgoing and backscattered photoelectron waves, when pairs are aligned, increases the peak amplitude above that expected for a single outgoing and backscattering event. The

two most intense scattering pathways (Figure 15) arise from Oct → Oct_1 → Oct_3 → Oct or inverse Oct → Oct_3 → Oct_1 → Oct third-order (χ_3) paths, and from the Oct → Oct_1 → Oct_3 → Oct_1 → Oct or inverse fourth-order (χ_4) path, where Oct is the central atom, Oct_1 belongs to the nearest cationic shell at 3.0 - 3.1 Å, and Oct_3 to the 3rd shell at 6.0 - 6.2 Å (Figure 15a). Oct_1 ↔ Oct ↔ Oct_1 χ_3 and χ_4-paths, in which the central Oct also actuates as a scatterer in the focusing geometry, are comparatively less intense. Figure 15b shows that none of these paths exist in dioctahedral structures as a result of the vacancy of one of the three octahedral sites involved in the focusing effect. The three Oct_3 atoms at twice the Oct-Oct_1 distance are separated from the central Oct atom by a vacancy site and, thus, their contribution is expected to be weak. This is precisely what is observed in Figure 13c where the intensity of peak H for Garfield nontronite is zero. As

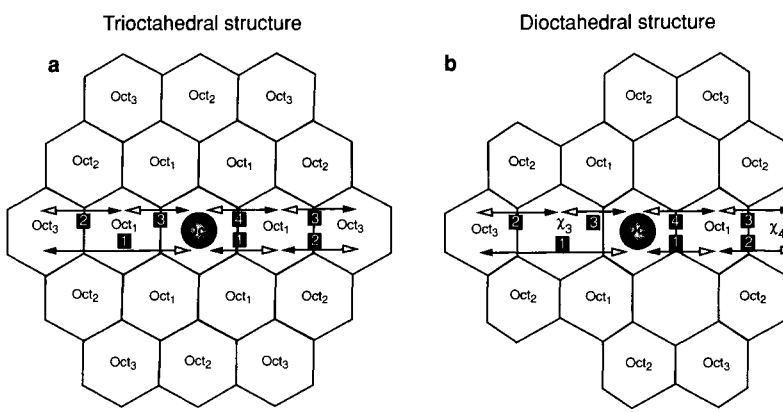

Figure 15. Distribution of cations in di- and trioctahedral sheets, and representation of most intense χ_3 and χ_4 multiple scattering paths. Dioctahedral sheets have no Oct-Oct_1-Oct_3 sequences and, consequently, the intensities of χ_3 and χ_4 MS paths are very low.

for the tilt of the basal O_4 shell, this second criterion for differentiating dioctahedral from trioctahedral structures can also be applied to powder EXAFS spectra. However, the sensitivity of polarization experiments is greater because of enhanced magnification of the octahedral sheet contribution in the parallel orientation. This increased sensitivity may be important for the study of clays with an intermediate di-, trioctahedral structure, i.e. for detecting the presence of small trioctahedral clusters within a dioctahedral framework (Manceau et al., 1999b).

Phyllomanganates

P-EXAFS experiments have been performed on monoclinic Na-exchanged birnessite (NaBi), on hexagonal H-birnessite (HBi) obtained by the low pH transformation of NaBi (Silvester et al. 1997), and on Co^{2+}-sorbed (pH 4) hexagonal birnessite (CoBi) (Manceau et al. 1997). The structure of monoclinic birnessite consists of edge-sharing MnO_6 octahedral sheets, with an average structural formula of $Na_{0.30}Mn^{2+}_{0.05}(Mn^{4+}_{0.74}Mn^{3+}_{0.21}\square_{0.05})O_{\sim 2\ 0.05}O_{\sim 2}$, where $\square$ denotes vacant structural sites (Figure 16a). Octahedral sheets contain Mn^{3+}-rich rows parallel to [010], which are separated from each other along [100] by two Mn^{4+} rows. The layer charge originating from Mn^{3+} for Mn^{4+} substitutions is predominantly compensated by exchangeable interlayer alkali or alkaline earth cations, but also by Mn^{2+}. The average structural formula of HBi at pH 5 is $Mn^{2+}_{0.05}Mn^{3+}_{0.116}(Mn^{4+}_{0.74}Mn^{3+}_{0.093}\square_{0.167})O_{1.7}(OH)_{0.3}$ (Drits et al. 1997b; Silvester et al. 1997). In contrast to the monoclinic form, HBi contains a considerable amount of octahedral vacancies, and its interlayer is devoid of exchangeable cations. Instead, corner sharing Mn^{3+} and Mn^{2+} octahedra are located above or below vacant sites (Figure 16b).

Polarized-RSFs for the various phyllomanganate samples are shown in Figure 17. The peaks labeled A, B, and C for NaBi and HBi correspond to the interactions between Mn-O, Mn-Mn_1 (edge-sharing octahedra), and Mn-Mn_2 (corner-sharing octahedra), respectively. The absence of peak C in NaBi is consistent with the absence, or scarcity, of corner-sharing octahedra in the monoclinic form, where manganese octahedra are almost exclusively edge linked (Figure 16a). Mn and Co K-edge P-RSFs for CoBi are similar, indicating that Mn and sorbed Co both fill layer and interlayer positions as represented in Figure 16c. Interestingly, in CoBi, Co^{2+} was shown to be oxidized by Mn^{3+} rather than by Mn^{4+}, and Co^{3+} then occupies layer and interlayer positions whereas non oxidized Co^{2+} remains sorbed above or below layer vacancy sites (Figure 16c) (Manceau et al. 1997).

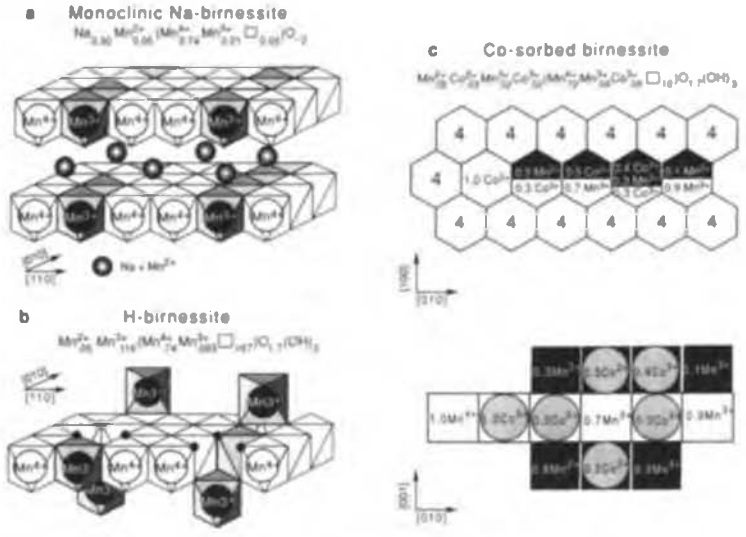

Figure 16. Idealized structures for monoclinic Na-exchanged birnessite (a), hexagonal H-rich birnessite (b) and Co-sorbed hexagonal birnessite (c). Structural formulae are written on a per octahedron basis. For c) projection in the ab and bc plane After Silvester et al. (1997) and Manceau et al. (1997).

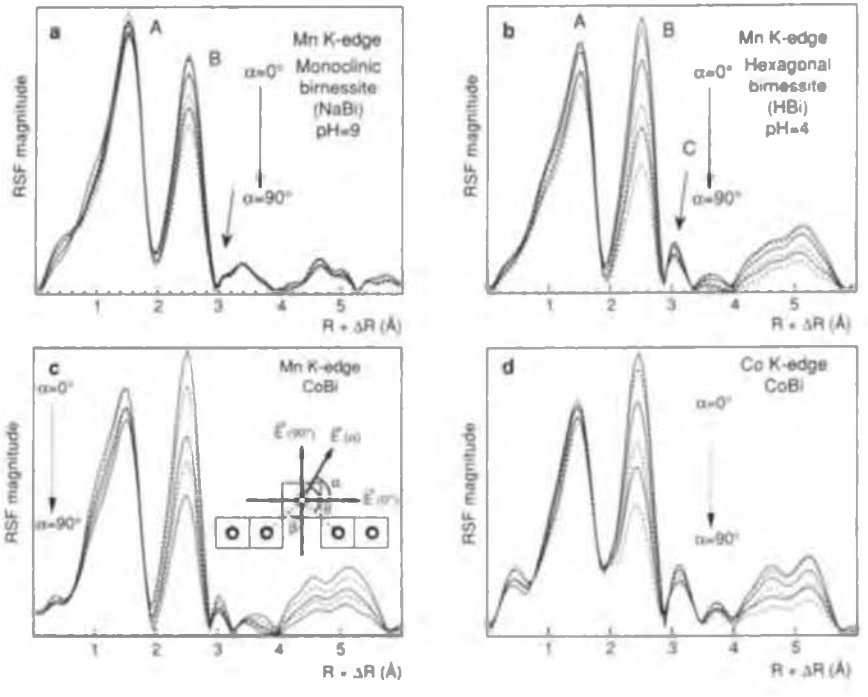

Figure 17. Polarized RSFs for NaBi (a), HBi (b), and CoBi (c,d). The 90° spectra have been calculated as discussed in the text.

Perfect orientation of crystallites within the various birnessite film preparations should result in a 90° spectrum in which there is no contribution from edge-sharing interactions (peak B), since under these conditions the electric field vector and the layer plane are orthogonal. Examination of Figure 17 shows that perfect parallel orientation of individual microcrystals within the film was never achieved for this group of minerals. The disorientation of microcrystals can be estimated from the reduction of amplitude of peak B upon changing the measurement angle from $\alpha = 0°$ to $\alpha = 90°$. This reduction amounts to 30% for NaBi, 54 % for HBi, and 55% and 60% at the Mn and Co K-edge of CoBi. Note that for CoBi, Co and Mn K-edge measurements logically provide very similar values, the small differences being attributed to some unidentified systematic effects. Figure 18 shows the {001} normalized pole figure for CoBi, with its corresponding ρ scan. The only orientation component is the <001> fiber texture, a now common observation for self-supporting films. But the maximal orientation density for this sample is fairly low (7.5 mrd) compared to Garfield nontronite (39 mrd, Fig 9), and the FWHM of the distribution of orientation is 32.2° of FWHM instead of 19.8° for Garfield. This difference accounts for the residual contribution of peak B in the normal orientation.

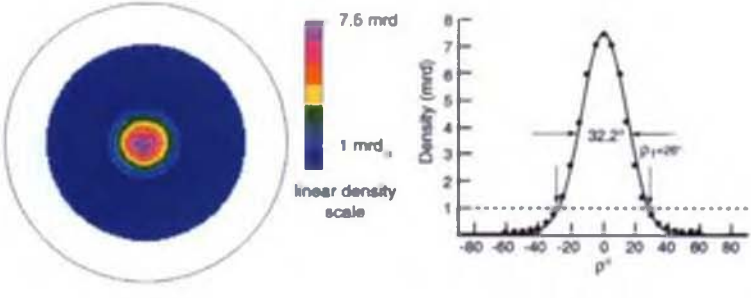

Figure 18. Experimental (001) pole figure and integrated ρ scan showing the angular dispersion of c* for the individual crystallites. The 1 mrd density level is represented by an horizontal dashed line.

Despite the poorer orientation of birnessite platelets within the film plane, critical information about the oxidation state of interlayer Mn and Co species in hexagonal birnessites can be obtained from the angular dependence of peak C (Figure 17). In CoBi, peak C decreases in amplitude as α increases, which indicates that $\beta >$ 54.7°. It is reasonable to assume that the β angle depends inversely on the size of sorbed cations, since larger ionic radii result in greater Mn-Oct_2 distances and, consequently, lower β values. So β should increase in the following order :

Mn^{2+} (0.83 Å) < Co^{2+} (0.745 Å) ≈ Zn^{2+} (0.74 Å) <

Mn^{3+} (0.645 Å) < Co^{3+} (0.545 Å) < Mn^{4+} (0.53 Å).

Since β = 53.5° in chalcophanite (Post and Appleman 1988; Wadsley 1955), it is likely that cations smaller than Zn would have a larger β value. Thus, a β value larger than 54.7° for CoBi points to the presence of Co^{3+} in the interlayer, because for Co^{2+} the β angle is expected to be similar to that of chalcophanite. Similarly, the angular dependence of peak C at the Mn K-edge of HBi and CoBi indicates that the ionic radius of Mn located at vacant sites is, on average, smaller than that of Zn^{2+}. The majority of manganese cations at these sites must therefore be Mn^{3+} or Mn^{4+} rather than Mn^{2+}, which is consistent with structural formulae (Figure 16). Also, if NaBi contained interlayer Mn^{2+} at vacant sites, Mn-Mn corner-sharing interactions would have been maximized in the 90° RSF since the ionic radius of Mn^{2+} is greater than Zn^{2+}. The absence of peak C in the 90° RSF allows us to conclude that there is very little, if any, corner-sharing manganese in NaBi. Clearly, any interlayer Mn^{2+} in NaBi does not sorb above or below lattice vacancy sites and must therefore occupy other specific interlayer sites.

CoOOH

Heterogenite (CoOOH) is a naturally occurring lamellar hydrated cobalt oxide (Hey 1962) of which two polytypes, 3R and 2H, have been described in the literature (Delaplane et al. 1969; Deliens and Goethals 1973). Two synthetic 3R samples (S1, S2) with different crystallinities have been studied by X-ray diffraction (XRD) and P-EXAFS. In Figure 19a it is seen that S1 and S2 have very similar XRD peak positions, and consequently unit cell parameters, but contrasting peak widths. Sample S2 has broader and weaker 10*l* reflections than S1, indicating a decrease of the three-dimensional (3D) ordering as a result of the presence of stacking faults and a decrease of the size of coherent scattering domains (CSDs) in the *c* direction. XRD patterns were simulated using structural parameters of the 3R polytype (Delaplane et al. 1969), and the nature and amount of crystalline defects were determined by using the mathematical

formalism described by Plançon (1981), Sakharov et al. (1982a; 1982b), and Drits and Tchoubar (1990). CSDs were assumed to have a disk-like shape of diameter Φ in the *ab* plane, and their size distribution along the *c* axis was quantified by two parameters, the average (N_{mean}) and maximum (N_{max}) number of layers (Reynolds 1989). The proportion of random stacking faults (W_R) in between adjacent 3-layer units was also determined. A

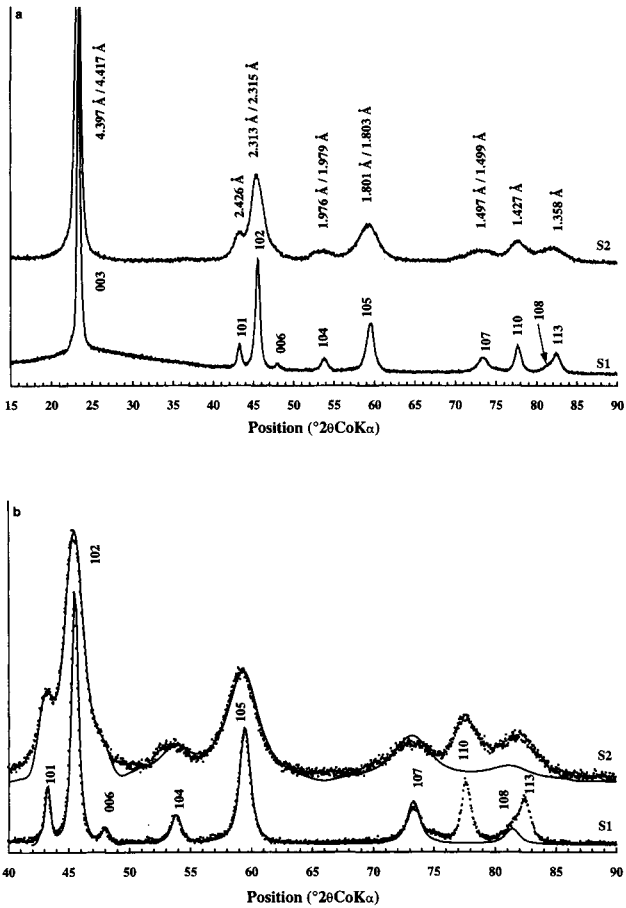

Figure 19. a) Experimental XRD pattern of synthetic CoOOH and indexing in a three-layer hexagonal unit cell (3R). a = 2.850 Å, c = 13.198 Å, γ = 120° for S1 and a = 2.855 Å, c = 13.200 Å, γ = 120°, for S2. When two d(hkl) values are given they refer to samples S1 and S2, respectively. b) Comparison between experimental (dots) and calculated (solid lines) XRD patterns. Only 10*l* lines were calculated. For S1, N_{mean} = 3, N_{max} = 12, Φ = 270 Å, W_R = 0%, and the proportion of Co vacancies is 15%. For S2, N_{mean} = 2, N_{max} = 5, Φ = 100 Å, W_R = 45%, and the proportion of Co vacancies is 8%. N is the number of 3-layer units stacked coherently.

good agreement between theory and experiment was obtained for S1 by assuming N_{mean} = 3, N_{max} = 12, Φ = 270 Å, W_R = 0%, and 15% of octahedral vacancies. For S2, optimal values were N_{mean} = 2, N_{max} = 5, Φ = 100 Å, W_R = 45%, and 8% of vacant sites (Figure 19b). These results indicate that S2 possesses a very defective structure both in the layer plane and in the perpendicular direction. In this sample, the probability of random displacement of two adjacent 3-layer units is as high as 0.45.

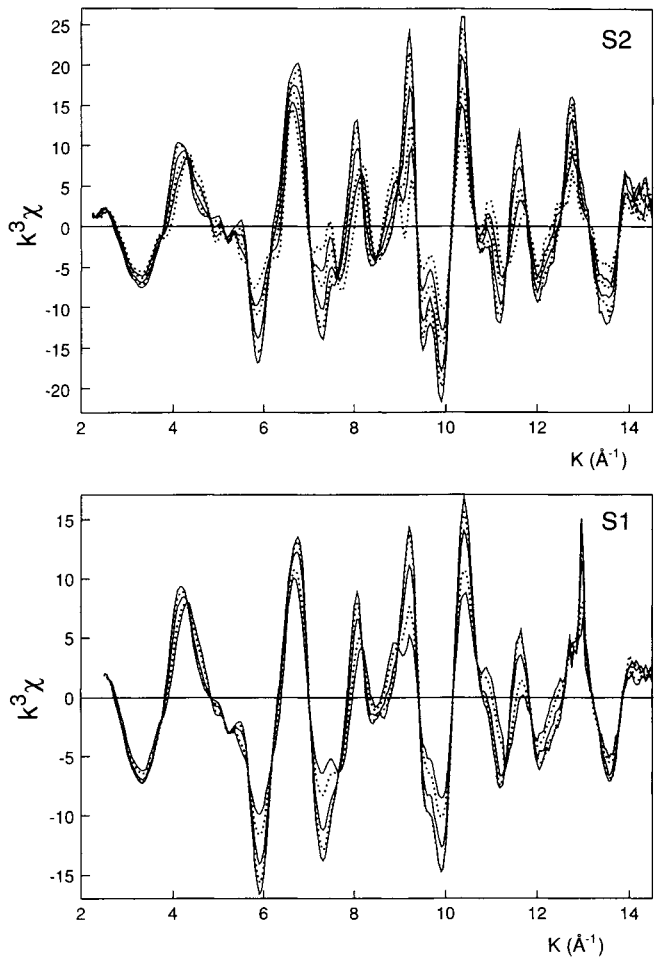

Figure 20. k^3-weighted Co K-edge P-EXAFS spectra for S1 and S2 at α angles of 0°, 20°, 35°, 50° (only for S1), and 60°. The 90° spectrum has been calculated using the method described in the text.). The amplitude of χ decreases with increasing α at 5.9, 7.3, 9.2, 10.4 Å^{-1}. Note the presence of isosbestic points where $\chi(k,\alpha)$ is independent of k.

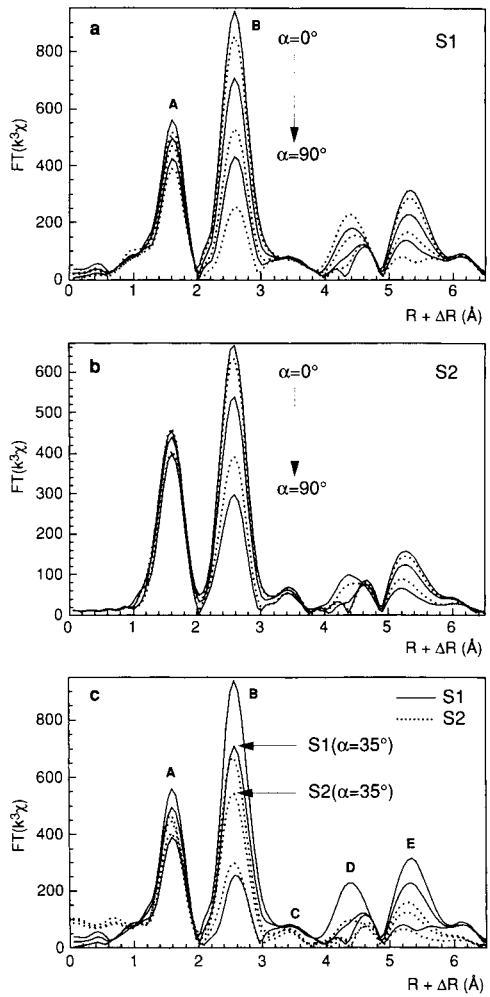

Figure 21. Co K-edge P-RSFs for S1 (a) and S2 (b) at α angles of 0°, 20°, 35°, 50° (only for S1), and 60°, derived from the EXAFS spectra shown in Figure 20. The 90° spectrum has been calculated. c) Comparison of S1 and S2 RSFs for α = 0°, 35°, and 90°. The amplitude decreases with increasing α.

Co K-edge P-EXAFS spectra and P-RSFs for the two CoOOH films are shown in Figure 20 and 21. A large angular dependence upon polarization is observed for the two samples, but it is more marked for S1. RSFs exhibit two major peaks denoted A and B at $R+\Delta R \approx 1.6$ and 2.6 Å. Peak A corresponds to the contribution of Co-$(O,OH)_1$ atomic

pairs, and peak B to Co-Co_1 pairs across octahedral edges (Figure 22). As for birnessite, perfect orientation of CoOOH layers should result in an out-of-plane spectrum in which there is no contribution from Co-Co layer pairs. In the heterogenite samples studied, the P-RSFs indicate that this contribution is not completely cancelled, most obviously for S2 (Figure 21b).

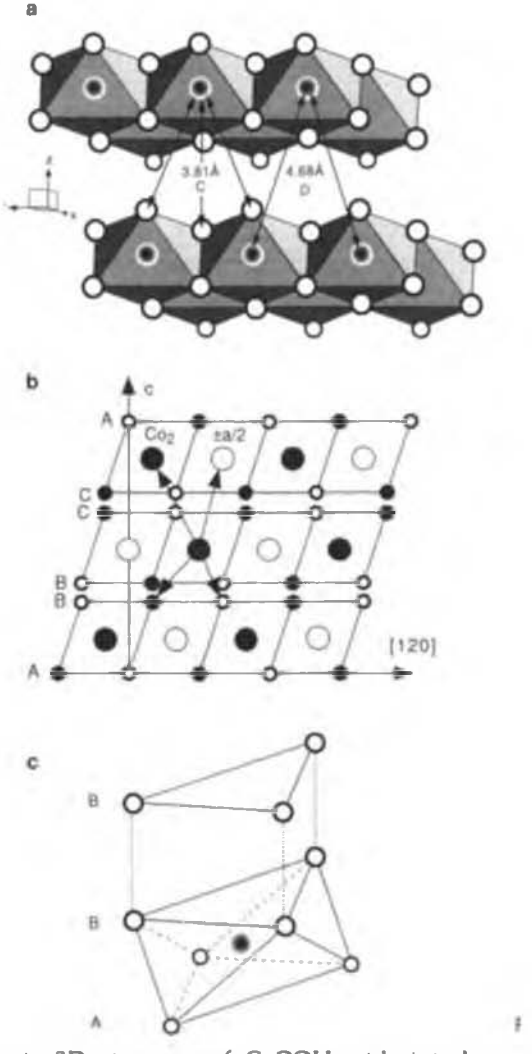

Figure 22. a) Schematic 3D structure of CoOOH with interlayer Co-O and Co-Co interactions at 3.81 Å and 4.68Å, respectively. b) projection of the 3R CoOOH structure down a. Open circles are atoms at ±a/2, dark circles are atoms at a=0. c) Schematic 3D representation of the -AB-B stacking of layers. Only lower O,OH sheet of the upper layer is shown. Dotted lines connect nearest O,OH of adjacent layers to display the prismatic stacking of the 3R polytype.

Examination of Figure 21c shows that S2 has a lower Co-Co_1 peak amplitude than S1 at $\alpha = 35°$. Since $\alpha = 35°$ is a magic angle, this difference does not originate from texture effects, but instead, results from differences in short-range order around Co in the two samples. The diminished amplitude of the S2 peak indicates a decreased coherence of observed Co-Co pairs. This result is consistent with the reduction of the CSD size in the *ab* plane measured by XRD for S2 (100 Å) compared to S1 (270 Å), although EXAFS and diffraction are not sensitive to the same distance scale. Co-$(O,OH)_1$ peaks have a similar amplitude, which means that the disorder of layers observed on Co-Co pairs does not significantly modify the symmetry of $Co(O,OH)_6$ octahedra. Further inspection of Figure 21c shows that S1 and S2 P-RSFs differ at $R + \Delta R = 4.4$ Å for $\alpha = 90°$. The prominent peak (D) observed in this orientation for S1 is absent for S2, and indicates that the two samples also differ in their out-of-plane structure. Owing to the possible importance of MS paths in this high R region (Manceau et al. 1998; O'Day et al. 1994), theoretical simulations are needed to interpret structurally this spectral dissimilarity.

P-EXAFS spectra for an ideal 3R CoOOH cluster were calculated *ab initio* by using the FEFF6 code (Rehr et al. 1992). All single scattering (SS) and MS contributions up to 8.4 Å from the central Co atom were computed. The total number of scattering paths is very large but only a small subset proved to be needed to completely reproduce the EXAFS features. The cut-off in magnitude of paths was set to 6% of the mean amplitude of the first backscattering shell. The many body reduction factor, S_0^2, is mostly independent of α (Bauer et al. 1996; Lederer et al. 1993) and was set to 0.85 (O'Day et al. 1994) for all spectra. The amplitudes of theoretical and experimental P-RSFs peaks for $\alpha = 35°$ were adjusted by optimizing Debye-Waller σ_j values. A minimum number of four σ_j values proved necessary to yield a good match between theory and experiment: $\sigma = 0.053$ Å for Co-$(O,OH)_1$, 0.059 Å for Co-Co_1, 0.07 Å for SS paths of more distant shells, and 0.08 Å for all MS paths. Note that σ of SS paths logically increases off the central atom.

Experimental and theoretical Fourier transforms (modulus and imaginary part) at $\alpha = 35.3°$ are contrasted in Figure 23a. This Figure shows that the four adjusted σ values sufficed in reproducing the experimental Fourier transform with a high degree of accuracy. The contributions from second (χ_2) and third + fourth (χ_{3-4}) order paths in the full RSF are compared in Figure 23b. The calculation of individual path contributions showed that RSFs are dominated by SS paths, MS being only significantly present in the $R + \Delta R = 5.3$ Å region. This long distance E peak arises from focusing scattering paths between layer Co atoms as has been discussed previously for phyllosilicates (Figure 15a), and should be more sensitive to the in-plane crystallinity

than the first Co peak (B) located at much shorter R + ΔR distance (2.6 Å). This is precisely what is observed experimentally since at α = 35° peak B is 25 % less intense in S2 than in S1, while peak E is halved in S2 compared to S1 (Figure 21c). Consequently, this multiple-scattering analysis provides additional evidence to the loss of structural order within S2 layers, and this result is in perfect agreement with the reduction of CSDs observed by XRD.

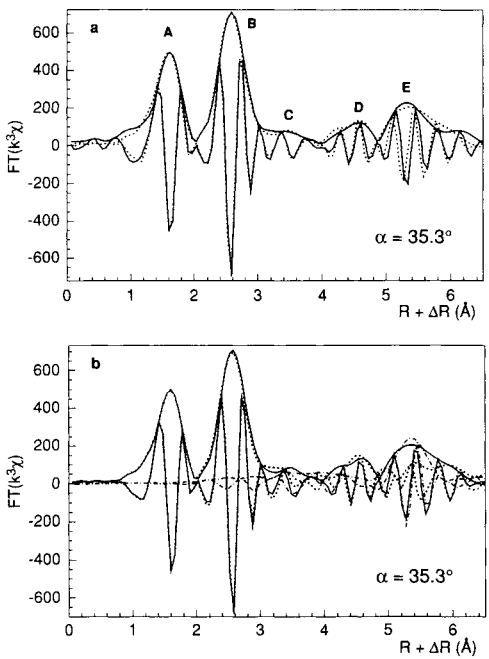

Figure 23. a) Comparison of S1 (solid line) and FEFF (dots) Fourier transforms for α = 35°. The envelope curves are the magnitude of the transforms (RSFs) and the fast oscillatory curves are the imaginary parts of the transforms. b) Fourier transform deconvolution of the relative contributions of single (χ_2, dotted line), multiple (χ_{3-4}, half-dotted line) and total (χ, solid line) scattering-paths calculated by FEFF for α = 35°.

P-RSFs computed for α=0°, 35°, and 90°, and the relative amplitudes of χ_2 and χ_{3-4} scattering pathways are presented in Figure 24. Figure 24a shows that the angular

dependence of P-RSFs observed experimentally (Figure 21a-c) is reproduced by FEFF calculations. As expected from the $\cos^2\alpha$ dependence of χ, the first Co-Co peak is zero at α=90° in the FEFF calculation. The nature of peaks C and D (Figure 21c) was determined by calculating the Fourier transforms of χ_2 and χ_{3-4} for both normal and perpendicular orientations (Figure 24b,c). The calculations showed that these peaks result from the SS contribution from nearest O and Co atoms of adjacent layers located at R = 3.81 Å and 4.68 Å (Co-Co_2 shell), respectively (Figure 22a). The mutual arrangement of successive

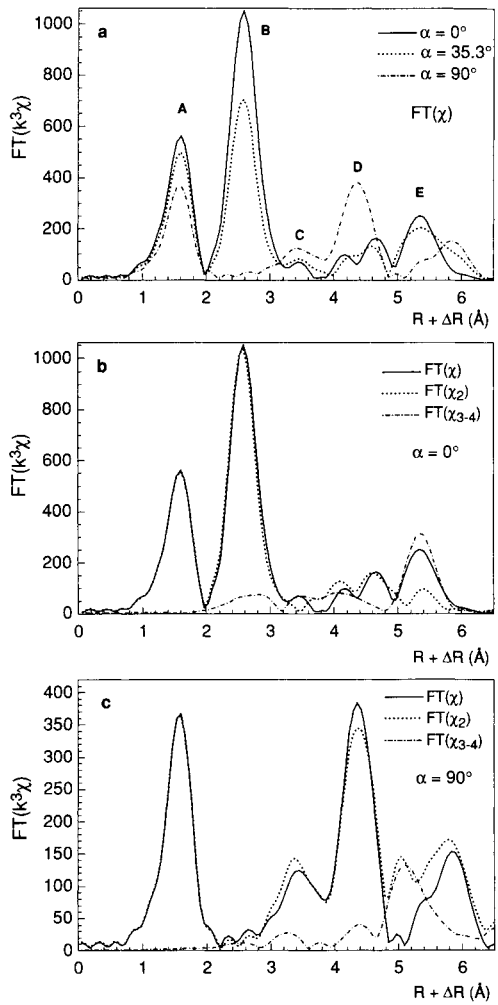

Figure 24. a) P-RSFs of FEFF spectra for α = 0°, 35.3°, and 90°. RSFs of single (χ_2), multiple (χ_{3-4}) and total (χ) scattering-paths for α = 0° (b) and α = 90° (c).

layers in this three-layer 3R polytype can be described by the usual close-packed notation A, B, C, and a, b, c in which capital letters stand for unequivalent crystallographic sites of O and OH groups, and lowercase letters for the positions of Co (Figure 22b). In this symbolic representation, the 3R layer stack can be denoted ...AcB-BaC-CbA... Anions from successive layers form prisms (Figure 22c) so that Co atoms are surrounded by 6 oxygens from the lower sheets of adjacent layers. Cation sheets have an hexagonal stack (... cab...) and, consequently, each Co has 6 Co_2 neighbors belonging to adjacent layers. The high number of nearest O and Co atoms in adjacent layers explains the high intensity of peak D and, to a lesser extent of peak C, at $\alpha = 90°$ (Figure 24). Peak D shows up more strongly and has a greater angular dependence than peak C because Co is a better backscatterer and the Co-Co_2 pair has obviously a lower β angle.

It comes from these considerations that P-EXAFS spectroscopy can be sensitive to the stacking mode of layered structures provided that the interlayer is unoccupied, otherwise the interlayer spacing is too large to detect the contribution from adjacent cations. This is the case for birnessite in which the interlayer is filled with either exchangeable (monoclinic form) or hydrolyzable (hexagonal form) cations resulting in an interlayer spacing of 7 Å or 10 Å compared to 4.4 Å in CoOOH. In the one-layer ...AcB-AcB-AcB... hexagonal structure of $Co(OH)_2$ (Brindley and Kao 1984; Lotmar and Feitknecht 1936) the Co_2 shell now contains only 2 cobalt (...ccc... cation stack) and the RSF of this 1H polytype is substantially different from that of 3R CoOOH (Manceau et al., 1999c). We can conclude from this detailed analysis that the decreased amplitude of peak D for S2 (Figure 21c) is caused by the loss of coherence of the Co-Co_2 shell as a result of the high density of defects in the c* direction. This result is fully consistent with XRD simulations, which showed that the probability of stacking faults between successive layers is as high as 0.45 in S2.

In edge-sharing octahedral structures, octahedra are generally flattened and the distortion is quantified by the flattening angle ψ (Figure 25a). This angle is defined as the angle between two diagonally opposite oxygens and the vertical (c* direction) (Bailey 1991). Apart from very distorted polyhedra, this angle is identical to the average β angle for the six Metal-(O,OH) pairs making up an octahedron. Consequently, ψ can be determined from the angular dependence of the first atomic shell contribution in P-EXAFS experiments. For a perfect octahedron, $\psi = 54.4°$ (Figure 25a) and the Metal-(O,OH) contribution will be invariant with a. Figure 21 shows that the amplitude of first RSF peaks decreases with increasing α, which indicates that $\psi > 54.7°$. For ideally

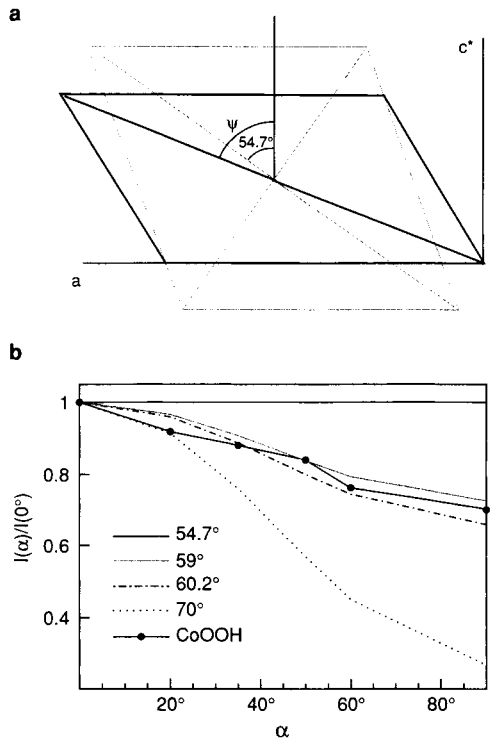

Figure 25. a) Projection of Co(O,OH) octahedron onto (010) before flattening (thin line) and after flattening (thick line). ψ is defined as the angle between c* and the line that connects opposite vertices of the octahedron. In a regular octahedron ψ = 54.4°, and it exceeds this value after flattening. b) Normalized intensity of Co-(O,OH) RSFs peaks as a function of α, and curves calculated for flattening angles of ψ = 54.7°, 59°, 60.2, and 70°.

self-supporting films, this angular variation is connected to α and ψ by (Manceau et al. 1998; Stöhr 1992)

$$\frac{I_\alpha}{I_0} = \frac{1 + \frac{3}{2}\sin^2\alpha(3\cos^2\psi - 1)}{1 - \frac{1}{2}(3\cos^2\psi - 1)} \qquad (13)$$

where I_α/I_0 represents peak intensities normalized to α = 0°. Experimental and calculated data for several ψ angles are compared in Figure 25b. The ψ = 60.2° angle

was chosen because it corresponds to the crystallographic CoOOH value, and the ψ = 70° angle in order to illustrate the good sensitivity of this method for evaluating ψ in an unknown sample. Examination of this figure shows that a precision on ψ of ~ 1° can be obtained, provided an ideal film orientation. Otherwise, $\psi_{exp.} < \psi_{cryst}$, and the method simply yields a minimum ψ value. In the present case, the simulation of experimental data for S2 yielded $\psi > 59°$, which is fairly close to the crystallographic value of 60.2°.

CONCLUSIONS

We have shown that the application of polarized EXAFS to highly ordered films prepared from fine-grained layered minerals can overcome many of the limitations associated with powder EXAFS studies. By exploiting the polarized nature of synchrotron radiation and measuring several spectra over multiple angles of the film relative to the electric field vector, it is possible to discern between overlapping in-plane and out-of-plane structural contributions, which permits extension of EXAFS spectra to true mid-range atomic distances. Thus, P-EXAFS allows us to study with greater precision the relative distribution of cations in the octahedral sheet of layered minerals, differentiate better between di-and trioctahedral phyllosilicates, quantify with improved resolution the surface structural chemistry of complex or poorly ordered layered minerals, and understand better the stacking order-disorder of layered materials.

ACKNOWLEDGMENTS

The authors thank Drs. Christa Bürgisser and Alan Stone for providing the CoOOH samples.

REFERENCES

Bailey SW. 1991. Hydrous phyllosilicates. Reviews in Mineralogy, Vol. 19, Washington DC: Mineralogical Society of America, 725 p.

Bauer ED, Bridges F, Booth CH, Boyce JB, Claeson T, Brorsson G, Suzuki Y. 1996. Local structure study about Co in $YBa_2(Cu_{1-x}Co_x)_3O_{7-d}$ thin films using polarized XAFS. Phys Rev B54: 13352-13360.

Brindley GW, Kao C-C. 1984. Structural and IR relations among brucite-like divalent metal hydroxides. Phys. Chem. Miner. 10: 187-191.

Brouder C. 1990. Angular dependence of X-ray absorption spectra. J. Phys. Cond. Matter 2: 701-738.

Bunge HJ. 1981. Textures in Materials Science. London: Butterworths.

Chateigner D, Wenk HR, Pernet M. 1997. Orientation analysis of bulk YBCO from incomplete neutron diffraction data. J. Appl. Cryst. 30: 43-48.

Delaplane RG, Ibers JA, Ferraro JR, Rush JJ 1969. Structure of CoOOH. J. Chem. Phys. 50: 1920 -1925.

Deliens M, Goethals H. 1973. Polytypism of heterogenite. Min. Mag. 39: 152-157.

Drits VA, Dainyak LG, Muller F, Besson G, Manceau A. 1997a. Isomorphous cation distribution in celadonites, glauconites and Fe-illites determined by infrared, Mossbauer and EXAFS spectroscopies. Clay Mineral. 32: 153-179.

Drits VA, Silvester E, Gorshkov AI, Manceau A. 1997b. The Structure of synthetic monoclinic Na-rich birnessite and hexagonal birnessite. Part 1. Results from X-ray diffraction and selected area electron diffraction. Am. Mineral. 82: 946-961.

Drits VA, Tchoubar C. 1990. X-ray diffraction by disordered lamellar structures: Theory and applications to microdivided silicates and carbons. Berlin: Springer Verlag, 371 p.

Fukushima Y, Okamoto T. 1987. Extended X-ray absorption fine-structure study of cobalt-exchanged sepiolite. In: Schultz LG, Van Olphen H, Mumpton FA, eds. Proc. Int. Clay Conf. Bloomington, Indiana: The Clay Minerals Society, 9-16.

Guttler B, Niemann W, Redfern SAT. 1989. EXAFS and XANES spectroscopy study of the oxidation and deprotonation of biotite. Miner. Mag. 53: 591-602.

Heald SM, Stern EA. 1977. Anisotropic x-ray absorption in layered compounds. Phys. Rev. B16: 5549-5559.

Hey MH. 1962. Cobaltic hydroxide in nature. Miner. Mag. 33: 253-259.

Lederer T, Arvanitis D, Tischer M, Comelli G, Troger L, Baberschke K. 1993. Structural determination of c(2x2)N/Cu(100): A multiple-scattering surface-EXAFS study. Phys. Rev. B48: 11277.

Lee JH, Guggenheim S. 1981. Single crystal X-ray refinement of pyrophyllite-1Tc. Am. Mineral. 66: 350-357.

Lotmar W, Feitknecht W. 1936. Structure of $Co(OH)_2$. Zeit. Krist. 93: 368-372.

Manceau A. 1990. Distribution of cations among the octahedra of phyllosilicates: insight from EXAFS. Can. Mineral. 28: 321-328.

Manceau A, Bonnin D, Kaiser P, Frétigny C. 1988. Polarized EXAFS of biotite and chlorite. Phys. Chem. Miner. 16: 180-185.

Manceau A, Bonnin D, Stone WEE, Sanz J. 1990. Distribution of Fe in the octahedral sheet of trioctahedral micas by polarized EXAFS. Comparison with NMR results. Phys. Chem. Miner. 17: 363-370.

Manceau A, Calas G. 1986. Ni-bearing clay minerals. 2. X-ray absorption study of Ni-Mg distribution. Clay Mineral. 21: 341-360.

Manceau A, Chateigner D, Gates W. 1998. Polarized EXAFS, distance-valence least-squares modeling (DVLS) and quantitative texture analysis approaches to the structural refinement of Garfield nontronite. Phys. Chem. Miner., 25, 347-365.

Manceau A, Decarreau A. 1988. Extended X-ray absorption fine-structure study of cobalt-exchanged sepiolite: Comment on a paper by Y. Fukushima and T. Okamoto. Clays Clay Mineral. 36: 382-383.

Manceau A, Drits VA, Silvester E, Bartoli C, Lanson B. 1997. Structural mechanism of Co(II) oxidation by the phyllomanganate, Na-buserite. Am. Miner. 82: 1150-1175.

Manceau A., Drits V.A., Lanson B., Chateigner D., Wu J., Huo D.F., Gates W.P., Stucki, J.W. 1999a. Oxidation-reduction mechanism of iron in dioctahedral smectites. 2. Structural chemistry of reduced Garfield nontronite. Submitted.

Manceau A., Lanson B., Drits V.A., Chateigner D., Gates W.P., Wu J., Huo D.F., Stucki J.W. 1999b. Oxidation-reduction mechanism of iron in dioctahedral smectites. 1. Structural chemistry of oxidized nontronite references. Submitted.

Manceau A., Schlegel M., K. Nagy, Charlet, L. 1999c. Evidence for the formation of trioctahedral clay upon sorption of Co^{2+} on quartz. Submitted.

McKale AG, Veal BW, Paulikas AP, Chan SK, Knapp GS. 1988. Improved ab initio calculatons for extended absorption fine structure spectroscopy. J. Amer. Chem. Soc. 110: 3763-3768.

Muller F, Besson G, Manceau A, Drits VA. 1997. Distribution of isomorphous cations within octahedral sheets in montmorillonite from Camp-Bertaux. Phys Chem Miner 24: 159-166.

O'Day PA, Rehr JJ, Zabinsky SI, Brown GE, Jr. 1994. Extended X-ray absorption fine structure (EXAFS) analysis of disorder and multiple-scattering in complex crystalline solids. J. Amer. Chem. Soc. 116: 2938-2949.

Plançon A. 1981. Diffraction by layer structure containing different kinds of layers and stacking faults. J. Appl. Cryst. 14: 300-304.

Post JE, Appleman DE. 1988. Chalcophanite, $ZnMn_3O_7{:}3H_2O$: New crystal-structure determination. Am. Miner. 73: 1401-1404.

Rehr JJ, Mustre de Leon J, Zabinsky SI, Albers RC. 1991. Theoretical X-ray absorption fine structure standards. J. Amer. Chem. Soc. 113: 5135-5145.

Rehr JJ, Zabinsky SI, Albers RC. 1992. High-order multiple-scattering calculations of X-Ray-absorption fine structure. Phys. Rev. Let. 69: 3397.

Reynolds RC, Jr. 1989. Diffraction by small and disordered crystals. In: Bish DL, Post JE, eds. Modern Powder Diffraction. Washington: Mineralogical Society of America, 145-181.

Sakharov BA, Naumov AS, Drits VA. 1982a. X-ray diffraction by mixed-layer structures with random distribution of stacking faults. Dokl. Akad. Nauk. SSSR 265: 339-343.

Sakharov BA, Naumov AS, Drits VA. 1982b. X-ray intensities scattered by layer structure with short range ordering parameters S≥1 and G≥1. Dokl. Akad. Nauk. SSSR 265: 871-874.

Sanz J, de la Calle C, Stone WEE 1984. NMR applied to minerals. V. The localization of vacancies of the octahedral sheet of aluminous biotites. Phys. Chem. Mineral 11: 235-240.

Schulz LG. 1949. A direct method of determining preferred orientation of a flat reflection sample using a Geiger counter X-ray spectrometer. J. Appl. Phys. 20: 1030-1033.

Silvester E, Manceau A, Drits VA. 1997. The Structure of synthetic monoclinic Na-rich birnessite and hexagonal birnessite. Part 2. Results from Chemical Studies and EXAFS Spectroscopy. Am. Miner. 82: 962-978.

Stöhr J. 1992. NEXAFS Spectroscopy. Berlin, Heidelberg: Springer-Verlag.

Stöhr J, Jaeger R. 1982. Absorption-edge resonances, core-hole screening, and orientation of chemisorbed molecules: CO, NO, and N2 on Ni(100). Phys Rev B26: 4111-4131.

Takeda H, Ross M. 1975. Mica polytypism: Dissimilarities in the crystal structures of coexisting 1M and 2M1 biotite. Am. Miner. 60: 1030-1040.

Wadsley AD. 1955. The crystal structure of chalcophanite, $ZnMn_3O_7.3H_2O$. Acta Cryst. 8: 1165-172.

Wenk HR. 1985. Measurement of pole figures. In: Wenk HR, eds. Preferred orientation in deformed metals and rocks. Orlando: Academic Press Inc., p. 11-47.

Wenk HR, Chateigner D, Pernet M, Bingert J, Hellstrom E, Ouladdiaf B. 1996. Texture analysis of Bi-2212 and 2223 tapes and wires by neutron diffraction. Physica C 272: 1-12.